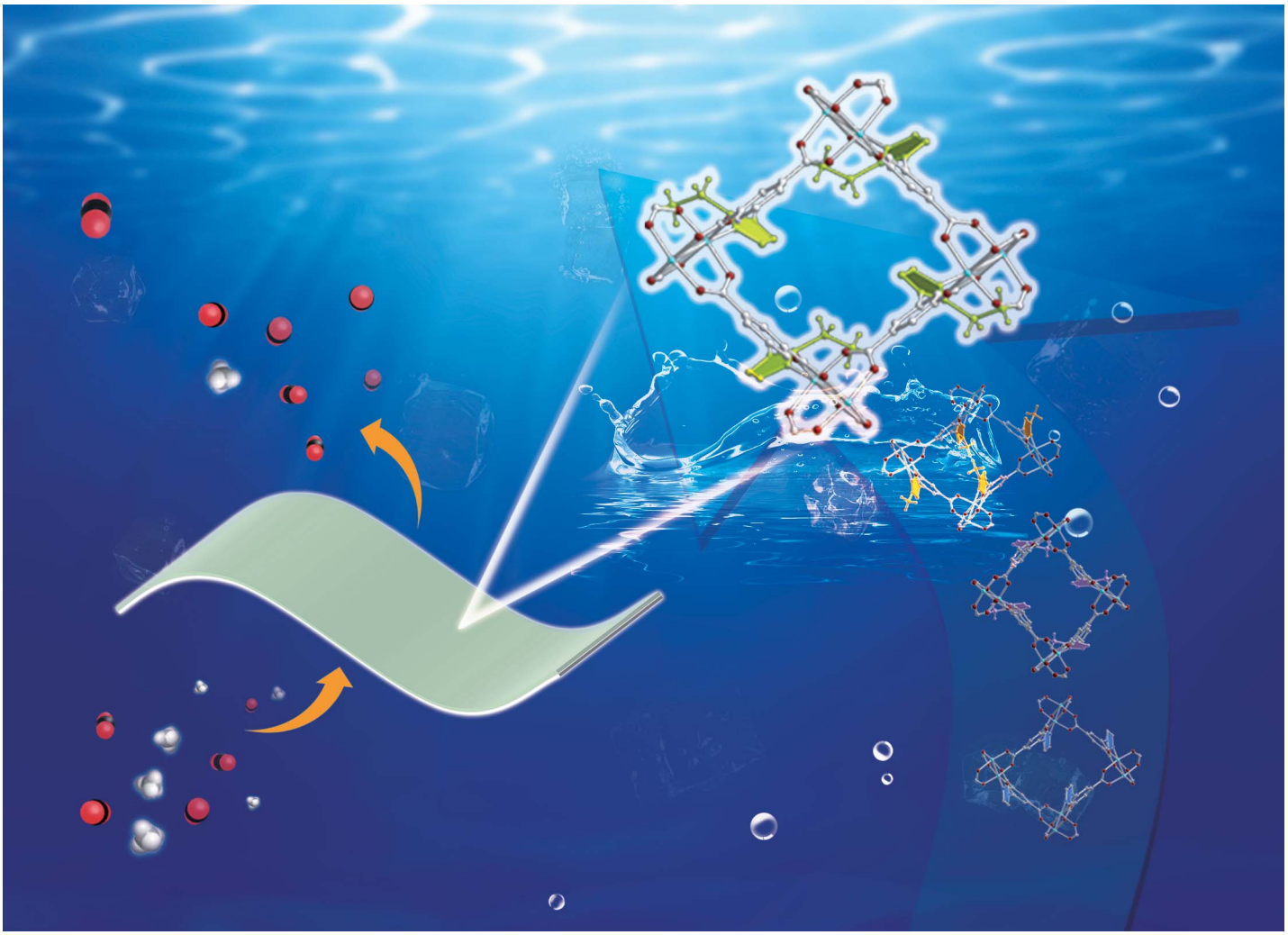

Showcasing a study on the fabrication of an optimal porous coordination polymer with alkyl groups for CH_4 purification by Asso. Prof. Jingui Duan, Prof. Wanqin Jin at the Nanjing Tech University and Prof. Susumu Kitagawa at Kyoto University.

Fine-tuning optimal porous coordination polymers using functional alkyl groups for CH_4 purification

By optimizing the position and length of the shortest two alkyl groups in the channels, a series of nano-porous PCPs were rationally designed and prepared. Among them, NTU-14 with pendant ethyl group showed excellent performance in adsorption- and membrane-based CH_4 purification.

As featured in:

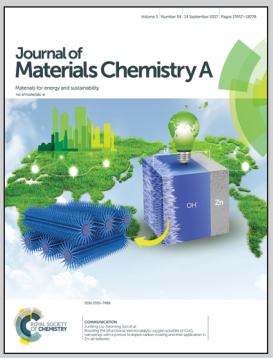

See Jingui Duan, Wanqin Jin, Susumu Kitagawa *et al.*, *J. Mater. Chem. A*, 2017, **5**, 17874.

ROYAL SOCIETY OF CHEMISTRY

rsc.li/materials-a

Registered charity number: 207890

Journal of Materials Chemistry A

PAPER

View Article Online
View Journal | View Issue

Cite this: J. Mater. Chem. A, 2017, 5, 17874

Fine-tuning optimal porous coordination polymers using functional alkyl groups for CH_4 purification†

Fujun Cheng,‡[a] Qianqian Li,‡[a] Jingui Duan,*[a] Nobuhiko Hosono,[b] Shin-ichiro Noro,[c] Rajamani Krishna,[d] Hongliang Lyu,[a] Shinpei Kusaka,[b] Wanqin Jin*[a] and Susumu Kitagawa*[b]

Received 30th March 2017
Accepted 2nd July 2017

DOI: 10.1039/c7ta02760e

rsc.li/materials-a

Nano-porous coordination polymers (nano-PCPs), as a new class of crystalline material, have become a lucrative topic in coordination chemistry due to the facile tunability of their functional pore environments. However, elucidating the pathways for the rational design and preparation of nano-PCPs with various integrated properties for feasible gas separation remains a great challenge. Here, we demonstrate a new route to achieve nano-PCPs with an integrated pore system and physical properties using a reticular chemistry strategy. By optimizing the position and length of the shortest two alkyl groups in the channels, unprecedented phenomena of improved surface area, gas uptake, gas selectivity, thermal stability and chemical stability were observed in the PCPs, especially in **NTU-14**, the structure with a pendant ethyl group. Furthermore, the high performance of adsorption- and membrane-based separation makes **NTU-14** a promising medium for CH_4 purification from a mixture at room temperature.

Introduction

Gas separation/purification from a mixture is a crucial and difficult process in industry.[1] Conventional strategies involve gas compression/cryogenic distillation, and require intensive energy for repeated gas evaporation and liquid condensation, as well as having high risk.[2] However, separation by means of adsorption and membrane technology using porous solids is recognized as a promising energy-efficient alternative. Older generation materials, including porous carbons, zeolites and ceramics, have been widely explored for gas separation.[3–7] However, further improvements in separation efficiency provide strong motivation to explore separation performance using a new generation of materials. Porous coordination polymers (PCPs), as a new class of crystalline material that allows the pre-design and precise integration of inorganic clusters and organic units into extended structures with periodic skeletons and ordered pore systems, are being intensively studied for gas separation.[8–18]

It is worth noting that despite the thousands of well-defined PCPs, a great challenge remains to fulfil the applications of such porous materials under feasible conditions.[19–22] Accompanying this focus on applications is a recognition of the need to improve PCPs to meet several important criteria: firstly, the accessible pore volume/surface area should allow efficient gas uptake under both static and dynamic conditions at room temperature; secondly, the PCPs should possess high capability for gas separation; thirdly, the structure should have good thermal and chemical stability under harsh conditions; finally and most importantly, the binding energy of the framework to gases should permit a completely reversible adsorption and desorption process with a low energy penalty.[23,24] Many PCPs can meet one or two of these prerequisites, but preparing a single domain with the above-mentioned compatible nature remains a great challenge.[25,26]

Recently, we introduced and developed a strategy by using an organic wall to prepare highly porous PCPs.[27] The generated framework, with hexagonal channels and a high resistance to water, acids and alkaline solutions (in particular at pH = 14 and 100 °C), demonstrated a promising future for the feasible application of CH_4 purification.[28] To further improve this work, we present a new route to achieve nano-PCPs with an integrated pore system and physical properties by optimizing the position and length of the shortest two alkyl groups in the channels. Based on **apo** topology, four new isostructures, named as **NTU-**

[a]State Key Laboratory of Materials-Oriented Chemical Engineering, College of Chemical Engineering, Jiangsu National Synergetic Innovation Centre for Advanced Materials, Nanjing Tech University, Nanjing 210009, China. E-mail: duanjingui@njtech.edu.cn; wqjin@njtech.edu.cn

[b]Institute for Integrated Cell-Material Sciences, Kyoto University, Yoshida, Sakyo-ku, Kyoto 606-8501, Japan. E-mail: kitagawa@icems.kyoto-u.ac.jp

[c]Research Institute for Electronic Science, Hokkaido University, Sapporo 001-0020, Japan

[d]Van't Hoff Institute for Molecular Sciences, University of Amsterdam, Science Park 904, 1098 XH Amsterdam, The Netherlands

† Electronic supplementary information (ESI) available: Synthesis and characterization of the four crystals, PXRD, TGA, IR, sorption isotherms, IAST, breakthrough calculations, fitting parameters and membrane preparation. CCDC 1533267–1533270. For ESI and crystallographic data in CIF or other electronic format see DOI: 10.1039/c7ta02760e

‡ These two authors contributed equally.

11, **NTU-12**, **NTU-13** and **NTU-14**, were prepared. The surface area, pore size and thermal and chemical stability of the PCPs were systemically tuned, and remarkably, **NTU-14** with a pendent ethyl group demonstrated optimal structural properties. Furthermore, as a solid absorbent and membrane material, **NTU-14** showed highly efficient CH_4 separation at room temperature.

Experimental section

The general procedures of the experiments and simulations can be found in the ESI.†

Synthesis of NTU-11 to NTU-14

Synthesis of NTU-11. H_3L^1 (4 mg), $CuBr_2$ (18 mg) and HBr (10 μL) were mixed with 2 mL of DMF/H_2O (4 : 1) in a 10 mL glass container, tightly capped with a Teflon vial, and heated at 80 °C for 48 h. After cooling to room temperature, the resulting green crystals were harvested and washed with DMF to give a high yield of ~75% (based on the ligand).

Synthesis of NTU-12. H_3L^2 (4 mg), $CuBr_2$ (18 mg) and HBr (30 μL) were mixed with 2 mL of DMF/H_2O (3 : 1) in a 10 mL glass container, tightly capped with a Teflon vial, and heated at 80 °C for 48 h. After cooling to room temperature, the resulting green crystals were harvested and washed with DMF to give a high yield of ~81% (based on the ligand).

Synthesis of NTU-13. H_3L^3 (4 mg), $CuBr_2$ (18 mg) and HBr (60 μL) were mixed with 2 mL of DMF/H_2O (3 : 1) in a 10 mL glass container, tightly capped with a Teflon vial, and heated at 80 °C for 48 h. After cooling to room temperature, the resulting green crystals were harvested and washed with DMF to give a high yield of ~73% (based on the ligand).

Synthesis of NTU-14. H_3L^4 (4 mg), $CuBr_2$ (18 mg) and HBr (10 μL) were mixed with 2 mL of DMF/H_2O (5 : 1) in a 10 mL glass container, tightly capped with a Teflon vial, and heated at 80 °C for 48 h. After cooling to room temperature, the resulting green crystals were harvested and washed with DMF to give a yield of ~62% (based on the ligand).

Results and discussion

Synthesis and structural characterization

The solvothermal reaction of copper(II) bromide ($CuBr_2$) with 5-imidazol-1-yl-isophthalic acid (H_3L^1) in *N*,*N*-dimethylformamide (DMF)/H_2O containing HBr afforded rod-shaped crystals in a high yield. Single-crystal X-ray studies show that the mother structure of $[Cu(L^1)]\cdot H_2O\cdot DMF$ (named as **NTU-11**) crystallizes in the space group $P2_1/c$ (Fig. 1 and Table S1†). The asymmetric unit of this framework includes one ligand and one Cu^{2+} ion only (Fig. S1†). Each ligand connects to three Cu paddlewheels, and each paddlewheel binds six ligands to enclose the rhombic nanotubes with benzene and imidazole rings serving as the corrugated walls (Fig. S2–S4†). These nanotubes extend infinitely along the *a*-axis, while the whole framework is established by sharing the adjacent tubes with the **apo**/alpha-PbO_2 topology (Fig. S21†). In this framework, the general open metal sites from the Cu paddlewheel are occupied by the coordination of nitrogen atoms from the imidazole motif, providing no specific active sites for possible ambient enthalpy in the channels. The channel has a size of about 5.3 × 6.2 Å^2 (defined by the diameters of the inserted interior contact atom), which is filled by disordered H_2O and DMF solvents in the as-synthesized phase. The solvents are established to be one H_2O and one DMF molecule per $Cu(L^1)$ unit by thermogravimetric analysis (TGA) with squeezed electrons. The estimated accessible volume of **NTU-11**, calculated using PLATON, reached 51.0% per unit cell, indicating good porosity.

Inspired by the structure of **NTU-11** and reticular chemistry, we found this to be a good platform for tuning the pore size and surface hydrophobicity by inserting alkyl groups at the imidazole motifs with varied positions (2′ and 4′) and chain lengths (–CH_3 to –CH_2CH_3) (Fig. 1). To fulfil this strategy, another three ligands were prepared by the reaction of 5-iodo-isophthalic acid dimethyl ester with a series of imidazole derivatives, followed by a hydrolysis reaction. Three rod-shaped crystals were then harvested in high yield from the solvothermal reaction between $CuBr_2$ and the corresponding ligands. As expected, single crystal X-ray studies confirmed that the three PCPs, **NTU-12** ($[Cu(L^2)]\cdot 1.5H_2O\cdot 1.5DMF$), **NTU-13** ($[Cu(L^3)]\cdot 1.5H_2O\cdot DMF$) and **NTU-14** ($[Cu(L^4)]\cdot 1.2H_2O\cdot DMF$), are isostructural **NTU-11** analogues. From the crystal data, all of the inserted alkyl groups were crystallographically resolved and exposed the inside channels (Fig. 1a). Compared to the mother structure of **NTU-11** (5.6 × 6.2 Å^2), the accessible channel size in **NTU-12** decreased to 5.1 × 5.8 Å^2. Significantly, the channel in **NTU-13** was divided into two equal parts (3.2 × 3.5 Å^2) after moving the methyl group from the 2′ to the 4′ position of the imidazole ring of the L^3 ligand. Furthermore, the ethyl group was introduced to the 2′ position of the imidazole ring in the L^4 ligand, to give a new PCP, **NTU-14**, with a reduced pore size of 4.3 × 4.8 Å^2 and a wrapped Cu cluster. Importantly, the bulk purity of the PCPs was confirmed by powder X-ray diffraction (PXRD) patterns and Le Bail analysis of the as-synthesized phase (Fig. S24, S25, S29, S30, S34, S35, S39 and S40†).

Static adsorption studies

Encouraged by the systemically tuned architectures, we explored the permanent porosities by N_2 adsorption. **NTU-11** to **14** exhibited the typical I isotherm characteristic of a microporous material (Fig. 2). However, **NTU-12**, **13** and **14**, with inserted alkyl groups, showed higher surface areas (BET (Langmuir): 1130 m^2 g^{-1} (1280 m^2 g^{-1}), 1000 m^2 g^{-1} (1260 m^2 g^{-1}) and 1058 m^2 g^{-1} (1200 m^2 g^{-1})) than that of their prototype, **NTU-11** (603 m^2 g^{-1} (698 m^2 g^{-1})) (Fig. 2a). However, as the lengths of the aliphatic chains decorating the pores in bio-MOF-11–14 increased, the BET surface areas decreased from 1148 m^2 g^{-1} to 17 m^2 g^{-1} in the bio-MOF-11 analogues.[24] In order to find a reason for this, the PXRD patterns of their activated and as-synthesized phases were studied. The diffraction peaks of (1 0 0) and (0 1 1) in the activated phase of **NTU-11** shifted to a high angle, while the PXRD patterns of the activated phase remained the same as those of their as-synthesized crystals for the other

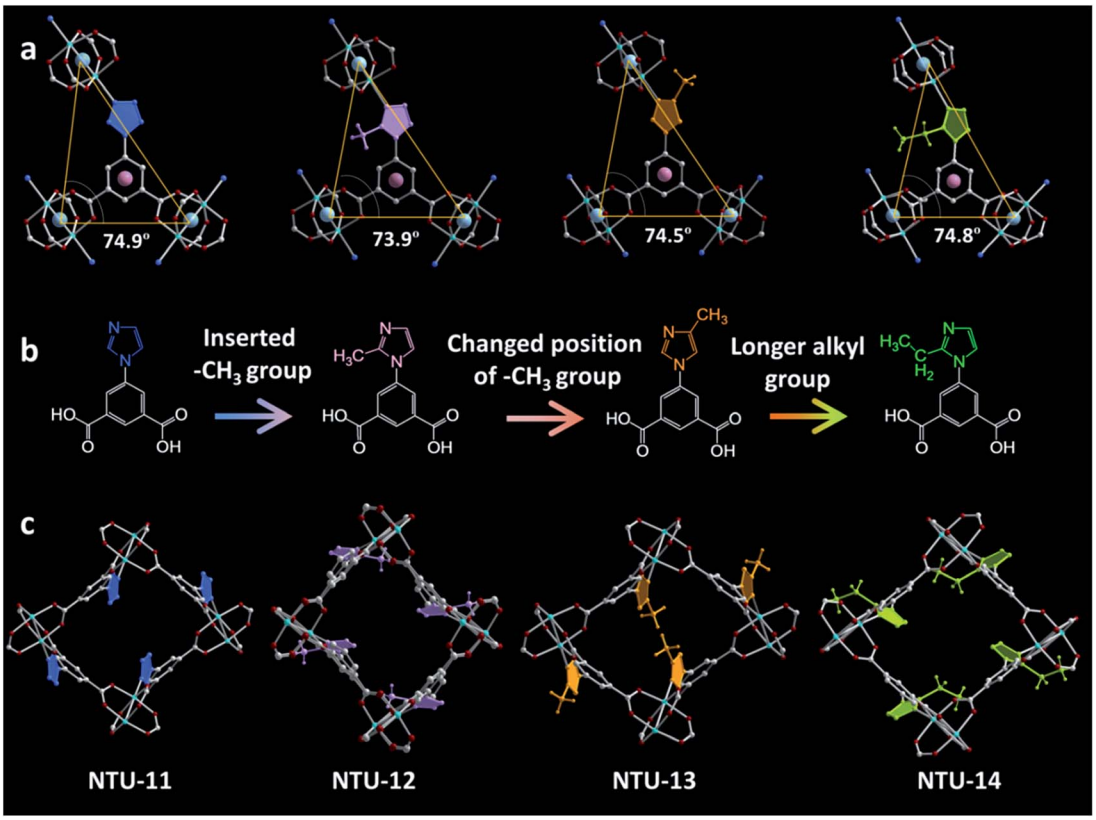

Fig. 1 Schematic showing the formation of the PCPs: (a) connection of the ligands; (b) evaluation of the ligands used for PCP construction; (c) position of the inserted alkyl groups in the corresponding channels and the systemically tuned window apertures in the PCPs. The modified parts of the ligands are highlighted in blue, pink, orange and green.

three PCPs, revealing the reduced pore parameters of **NTU-11** after activation (Fig. S29, S34 and S39†).

The increase in the basicity of the imidazole nitrogen, through the addition of the $-CH_3$ or $-CH_2CH_3$ group, makes the structure more attractive to Cu ions, reflecting the enhanced strength of the coordination bonds in **NTU-12**, **13** and **14**. In other words, covalent modification of the additional alkyl groups is not only theoretically reducing the pore surface area, more importantly, is conducive to the establishment of a stable structure, in particular the fully activated network.

Due to the higher surface areas of **NTU-12** to **14**, we evaluated their channel functions that were induced by the varied positions and lengths of the alkyl groups. Single component gas-adsorption isotherms of a series of energetic gases (CO_2, CO, CH_4, C_2H_4 and H_2) in **NTU-12**, **13** and **14** were collected at multiple temperatures (Fig. S42–S52†). The total CO_2 uptakes of the PCPs are close to each other (13.4 to 16 wt%) at 1 bar and 298 K (Fig. 2b). However, **NTU-13** (7.7 wt%) shows an uptake of CO_2 two times higher than those of **NTU-12** (3.8 wt%) and **14** (3.8 wt%) at 0.15 bar. Remarkably, the CO_2 uptake for **NTU-13** at 298 K and 0.15 bar is larger than those of well-known PCPs with functional sites, such as bio-MOF-11 (5.4 wt%),[29] NJU-Bai8 (5.4 wt%),[30] ZIF-8 (3.3 wt% (ref. 31)) and MIL-53(Al) (3.1 wt%),[32] and comparable to the performance of NJU-bai7 (8.0 wt%).[30] Compared to the conventional strategies using inserted amide groups or exposed open metal sites, this is the first time such a significant uptake improvement has been demonstrated in PCPs, just by changing the position of the methyl group without changing the accessible pore surface area and volume. This can be explained by the higher values of adsorption enthalpy (Q_{st}), derived from the narrower window aperture in **NTU-13** (Fig. 2b inset). Additionally, similar C_2H_4 adsorption in the PCPs was also found, however, in contrast to this, the uptake of CH_4 increased very slowly with pressure, indicating their potential to be used for separation.

Dynamic adsorption studies

Dynamic adsorption uptake is an important factor that can influence the PSA process.[33] Thus, we evaluated the temperature-dependent gravimetric adsorption cycling performance of **NTU-12**, **13** and **14** with CO_2 using TGA technology (Fig. 3). After heating the evacuated samples at 373 K for 100 min, the samples were cooled to 308 K and the temperature was maintained for 5 min. A mass change of around 4.6 wt% was observed in **NTU-12**, and this value increased to 6.7 wt% and 9.2 wt% in **NTU-14** and **13**, respectively. In contrast to the static adsorptions at 298 K, **NTU-14** reverses the trend and shows better performance of dynamic adsorption, while the bigger increase in the performance of **NTU-13** compared to that of **NTU-12** confirms the high importance of the length of the alkyl groups (from methyl to ethyl) and the position of the

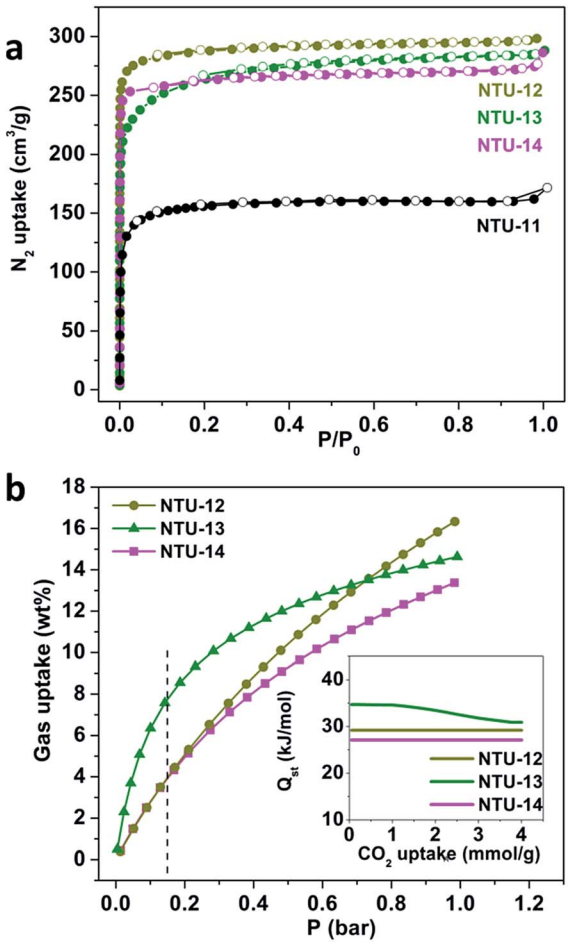

Fig. 2 (a) N_2 adsorption isotherms of **NTU-11** to **14** at 77 K. (b) CO_2 adsorption isotherms of **NTU-12** to **14** at 298 K; the inset image shows the calculated Q_{st} values of **NTU-12** to **14**. All isotherms are reversible. Desorption points were omitted for clarity.

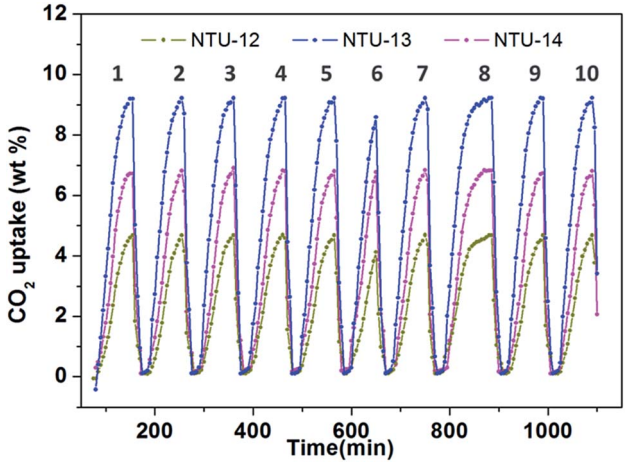

Fig. 3 Dynamic adsorption studies of CO_2 in **NTU-12**, **13** and **14**. The flow rates are 50 mL min^{-1}. The sample mass was normalized to 0% and max% at 373 K and 308 K, respectively.

methyl group (from 2′ to 4′ of the imidazole) for dynamic adsorption. Importantly, after five cycles, we reduced the equilibrium time from 10 to 1 min and extended it from 10 to 30 min in the sixth and eighth cycles, respectively. The gas uptakes for all of the PCPs decreased very slightly in the sixth cycle and remained the same in the eighth. Once the equilibrium was reversed, such as in cycles 7 and 9, the gas uptake of all of the PCPs was fully recovered. The long term experiments therefore reflect that **NTU-13** and **NTU-14** have high capabilities for CO_2 capture under kinetic flowing gas conditions.

Thermal and chemical stability

With such promising observations, we explored the thermal and chemical stability of the PCPs, as these are another two important factors for determining their feasible applications. Thermogravimetric analysis (TGA) showed that all of them exhibited weight loss before 200 °C and plateau ~300 °C. Due to the limited information provided by TG technology, we then performed varied temperature PXRD experiments on each of the PCPs under an N_2 atmosphere. As shown in Fig. 4, the (1 0 0) and (0 1 1) peaks of **NTU-11** became broader and also shifted to a high angle before 200 °C. However, **NTU-12** and **13** kept their original X-ray diffraction pattern, even at an increased temperature (240 °C), and a similar trend was observed at a higher temperature for **NTU-14** (280 °C). In sharp contrast, a series of NbO-type PCPs with different dialkoxy-substituents showed decreased thermal stability as the side chain length increased.[34] An explanation for the thermal stability changes in **NTU-11** to **14** should be that the short alkyl groups allow for less movement and also enhance the strength of the coordination bonds in their crystal structures with the input of thermal energy.

For the initial water/chemical stability evaluation, as-synthesized crystals of each PCP were soaked in water for 24 h at 298 K. As evidenced by PXRD (Fig. S26, S31, S36 and S41†), the crystalline arrangement of **NTU-11** changed a lot. In contrast, **NTU-12** dissolved partially and **NTU-13** kept its original phase after two weeks of water corrosion. More importantly and remarkably, **NTU-14**, with a functional ethyl group, showed well-matched crystalline diffractions after two months of treatment. Encouraged by this, we further examined the chemical stability of **NTU-14** in chemical solutions (HCl for pH = 2 and NaOH for pH = 12) at room temperature. The PXRD patterns showed no loss of crystallinity, while the N_2 adsorption (77 K) of chemically treated **NTU-14** (at pH = 2 and 7) is the same as that of the fresh sample in terms of both shape and total capacity, reflecting its good acid stability (Fig. 5 and S41†). With the crystal structures in mind, the high aqueous and chemical stability of **NTU-14** could be ascribed to the protection of the copper cluster coordination geometry by the hydrophobic ethyl group, as well as the stronger coordination of Cu–N. By combining the tuned thermal and chemical stability of the four PCPs, we found for the first time, to the best of our knowledge, that the insertion of two small alkyl groups can simultaneously improve the thermal stability and water/chemical stability of highly porous PCPs, indicating that not only electronic but also steric effects on the metal ion environment are important. In contrast to **NTU-11**, alkyl-modified **NTU-12**, **13** and **14** showed good framework stability toward SO_2 treatment. However, only **NTU-14**, with its pendant ethyl group, kept its original and

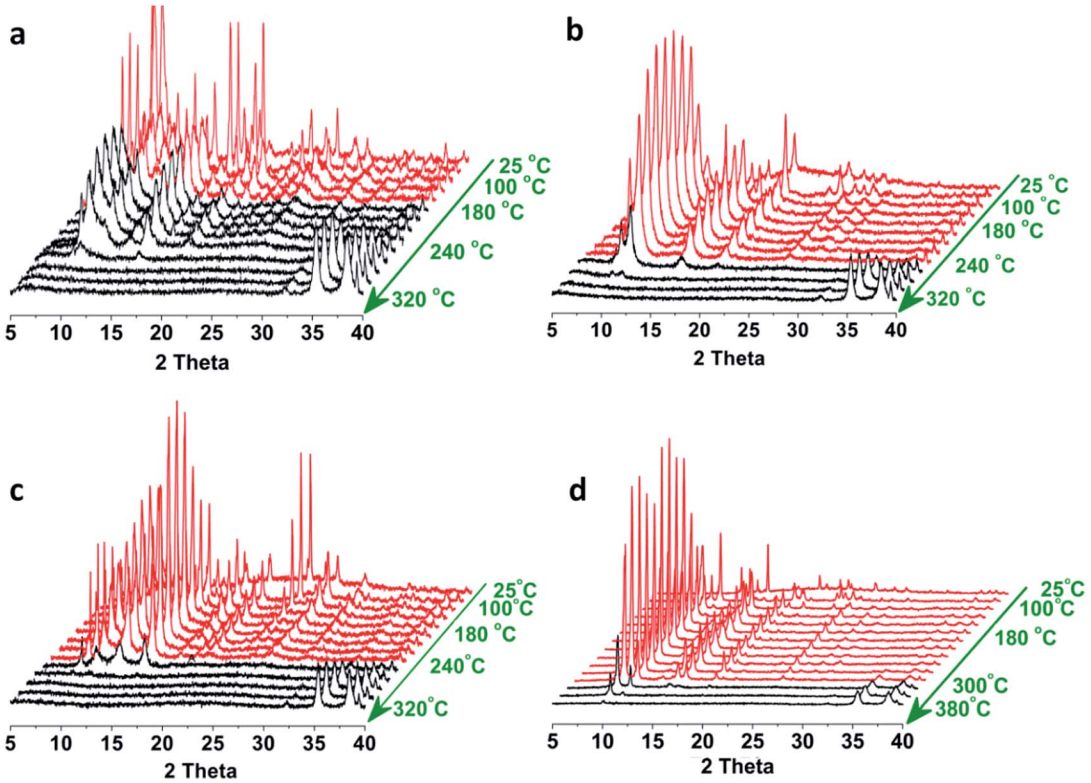

Fig. 4 Varied temperature PXRD patterns of NTU-11 (a), 12 (b), 13 (c) and 14 (d) under an N_2 atmosphere. The PXRD patterns highlighted in red indicate the maintained structures at the corresponding temperatures. The thermal stability gradually increased from (a) to (d).

highly crystalline phase under water vapour treatment (60 °C, 24 h) (Fig. S54†).

Co-adsorption and membrane separation

With integrated structural properties, **NTU-14** was selected to evaluate the ability for adsorption- and membrane-based CH_4 separation. We performed a trial co-adsorption experiment by dosing a C_2H_4 and CH_4 mixture at 298 K. The results showed that C_2H_4 was selectively adsorbed from the C_2H_4/CH_4 mixture as the gas composition of the adsorbed component is 97.2/2.8, whereas the dosing gas composition is 50/50. The partition coefficient indicates the high preferential adsorption of C_2H_4 in the presence of CH_4. Meanwhile, the high working capacities (46.7 $cm^3\ g^{-1}$) make it suitable for CH_4 purification from a mixture (Fig. 6). To better understand the adsorption-based separation, adsorption enthalpies were calculated. **NTU-14** exhibits a strong binding affinity for C_2H_4 (~35 kJ mol^{-1}), which is higher than that of **NTU-12** (~30 kJ mol^{-1}). The values are practically independent of gas loading, indicating the average interactions that are generated, principally from the organic part of the PCP and the guest molecule. In contrast, **NTU-14** shows a relatively low CH_4 adsorption enthalpy (~21 kJ mol^{-1}) (Fig. S52†).

Additionally, membrane processes are unique alternatives that recently have gained much attention. Therefore, **NTU-14** particles were incorporated into polyether-*block*-amide (PEBA) to prepare a mixed matrix membrane (MMM) (see ESI:† membrane preparation). The **NTU-14**/PEBA membrane with a light green colour is flexible enough to be curved (Fig. S55a and b†). The cross-sectional and top view of **NTU-14**/PEBA showed that the **NTU-14** particles were well-dispersed in the polymer matrices (2 μm thickness and 3.2 cm radius) without fractures (Fig. S55c and d†). The PXRD pattern of **NTU-14**/PEBA was collected and is shown in Fig. S54e.† The diffraction peaks of the MMMs are consistent with the combination of simulated data for **NTU-14** and the PEBA polymer, indicating the intact structure of **NTU-14** even after the membrane formation process. To guarantee the reliability of the results, the

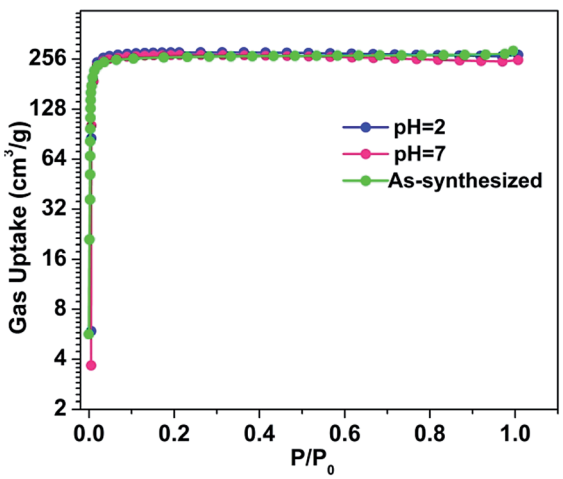

Fig. 5 N_2 adsorption of water/chemical treated NTU-14 at 77 K.

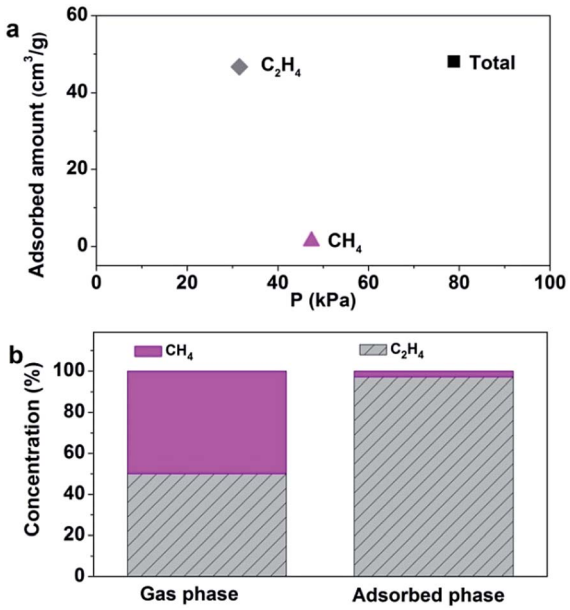

Fig. 6 Results of the co-adsorption experiment obtained by flushing a 50/50 mixture of C_2H_4/CH_4 over **NTU-14** at 298 K (a), followed by ascertaining the composition of the adsorbed phase, detected by gas chromatography (b).

measurements were repeated on four different membranes. A single gas permeation test using a constant volume/variable pressure technique was performed on the MMMs at 0.35 MPa and room temperature. **NTU-14**/PEBA shows improved CO_2 permeability over the bare polymer (from 4.5 to 5.6 GPU), coupled with a decrease in the permeability of CH_4, from 0.2 GPU in the bare polymer membrane to 0.16 GPU in the MMM. Thus, the ideal separation factor of CO_2/CH_4 showed improvement from ~22 up to ~34, which was 1.5 times higher than that of the neat PEBA membrane (Fig. S56†). More interestingly, long term tests showed that both the CO_2 permeability and CO_2/CH_4 selectivity can be retained as those of the initial stage for 120 h (Fig. S56c†). Therefore, by combining these attractive properties, despite some recent works, **NTU-14** remains one of the most optimal PCPs for feasible CH_4 purification.

Conclusions

Inspired by reticular chemistry, we demonstrate a new route to prepare nanoporous PCPs with an optimal pore system and physical properties by utilizing alkyl-modified low symmetry ligands and Cu dimers. With increased surface area, unprecedented phenomena of improved gas uptake, gas selectivity, thermal stability and chemical stability were observed by inserting a methyl group at different positions on the ligands, or varying the length from a methyl to an ethyl group in the PCPs. Remarkably, these promising advantages can be well integrated into one crystal domain, **NTU-14**, with an exposed ethyl group in the channels. Furthermore, co-adsorption and membrane experiments showed that **NTU-14** is one of the most optimal media for feasible CH_4 purification. Thus, we envisage that our work here will not only provide some examples with versatile structures and promising applications, but also will open the path for the deeper investigation of alkyl functionalities in PCP chemistry.

Acknowledgements

We thank the financial support of the National Science Foundation of China (21301148 and 21671102), National Science Foundation of Jiangsu Province (BK20161538), and Innovative Research Team Program by the Ministry of Education of China (IRT13070), Six talent peaks project in Jiangsu Province (JY-030) and the State Key Laboratory of Materials-Oriented Chemical Engineering (ZK201406). N. H. and S. K. acknowledge the KAKENHI Grant-in-Aid for Specially Promoted Research (No. 25000007) from the Japan Society of the Promotion of Science (JSPS).

References

1 J. Y. Lin, *Science*, 2016, **353**, 121–122.
2 C. A. Grande, S. Cavenati, F. A. Da Silva and A. E. Rodrigues, *Ind. Eng. Chem. Res.*, 2005, **44**, 7218–7227.
3 A. F. Ismail and L. I. B. David, *J. Membr. Sci.*, 2001, **193**, 1–18.
4 K. Keizer and H. Verweij, *CHEMTECH*, 1996, **26**, 37–41.
5 R. Soria, *Catal. Today*, 1995, **25**, 285–290.
6 F. S. Su, C. Y. Lu, S. C. Kuo and W. T. Zeng, *Energy Fuels*, 2010, **24**, 1441–1448.
7 V. Goetz, O. Pupier and A. Guillot, *Adsorption*, 2006, **12**, 55–63.
8 E. D. Bloch, W. L. Queen, R. Krishna, J. M. Zadrozny, C. M. Brown and J. R. Long, *Science*, 2012, **335**, 1606–1610.
9 H. Sato, W. Kosaka, R. Matsuda, A. Hori, Y. Hijikata, R. V. Belosludov, S. Sakaki, M. Takata and S. Kitagawa, *Science*, 2014, **343**, 167–170.
10 C. E. Wilmer, O. K. Farha, Y. S. Bae, J. T. Hupp and R. Q. Snurr, *Energy Environ. Sci.*, 2012, **5**, 9849–9856.
11 S. Kitagawa, R. Kitaura and S. Noro, *Angew. Chem., Int. Ed.*, 2004, **43**, 2334–2375.
12 H. Furukawa, N. Ko, Y. B. Go, N. Aratani, S. B. Choi, E. Choi, A. O. Yazaydin, R. Q. Snurr, M. O'Keeffe, J. Kim and O. M. Yaghi, *Science*, 2010, **329**, 424–428.
13 O. K. Farha, A. O. Yazaydin, I. Eryazici, C. D. Malliakas, B. G. Hauser, M. G. Kanatzidis, S. T. Nguyen, R. Q. Snurr and J. T. Hupp, *Nat. Chem.*, 2010, **2**, 944–948.
14 D. Q. Yuan, D. Zhao, D. F. Sun and H. C. Zhou, *Angew. Chem., Int. Ed.*, 2010, **49**, 5357–5361.
15 J. P. Zhang, Y. B. Zhang, J. B. Lin and X. M. Chen, *Chem. Rev.*, 2012, **112**, 1001–1033.
16 G. K. H. Shimizu, J. M. Taylor and S. Kim, *Science*, 2013, **341**, 354–355.
17 M. Hirscher, *Angew. Chem., Int. Ed.*, 2011, **50**, 581–582.
18 D. Tian, Q. Chen, Y. Li, Y. H. Zhang, Z. Chang and X. H. Bu, *Angew. Chem., Int. Ed.*, 2014, **53**, 837–841.
19 H. Furukawa, K. E. Cordova, M. O'Keeffe and O. M. Yaghi, *Science*, 2013, **341**, 974–986.

20 P. Nugent, Y. Belmabkhout, S. D. Burd, A. J. Cairns, R. Luebke, K. Forrest, T. Pham, S. Q. Ma, B. Space, L. Wojtas, M. Eddaoudi and M. J. Zaworotko, *Nature*, 2013, **495**, 80–84.

21 G. Mouchaham, L. Cooper, N. Guillou, C. Martineau, E. Elkaim, S. Bourrelly, P. L. Llewellyn, C. Allain, G. Clavier, C. Serre and T. Devic, *Angew. Chem., Int. Ed.*, 2015, **54**, 13297–13301.

22 Q. Y. Yang, S. Vaesen, F. Ragon, A. D. Wiersum, D. Wu, A. Lago, T. Devic, C. Martineau, F. Taulelle, P. L. Llewellyn, H. Jobic, C. L. Zhong, C. Serre, G. De Weireld and G. Maurin, *Angew. Chem., Int. Ed.*, 2013, **52**, 10316–10320.

23 J. G. Duan, M. Higuchi, R. Krishna, T. Kiyonaga, Y. Tsutsumi, Y. Sato, Y. Kubota, M. Takata and S. Kitagawa, *Chem. Sci.*, 2014, **5**, 660–666.

24 T. Li, D. L. Chen, J. E. Sullivan, M. T. Kozlowski, J. K. Johnson and N. L. Rosi, *Chem. Sci.*, 2013, **4**, 1746–1755.

25 Y. B. He, R. Krishna and B. L. Chen, *Energy Environ. Sci.*, 2012, **5**, 9107–9120.

26 S. Negishi, Y. Sato, M. Dan, G. Hamanaka, Y. Kosugi, K. Kobayashi, M. Ohara, W. Hatsuse, R. Furukawa and H. Kaneko, *Zool. Sci.*, 2005, **22**, 1450.

27 J. G. Duan, W. Q. Jin and S. Kitagawa, *Coord. Chem. Rev.*, 2017, **332**, 48–74.

28 J. G. Duan, M. Higuchi, S. Horike, M. L. Foo, K. P. Rao, Y. Inubushi, T. Fukushima and S. Kitagawa, *Adv. Funct. Mater.*, 2013, **23**, 3525–3530.

29 J. An, S. J. Geib and N. L. Rosi, *J. Am. Chem. Soc.*, 2010, **132**, 38–39.

30 L. T. Du, Z. Y. Lu, K. Y. Zheng, J. Y. Wang, X. Zheng, Y. Pan, X. Z. You and J. F. Bai, *J. Am. Chem. Soc.*, 2013, **135**, 562–565.

31 R. Banerjee, H. Furukawa, D. Britt, C. Knobler, M. O'Keeffe and O. M. Yaghi, *J. Am. Chem. Soc.*, 2009, **131**, 3875–3877.

32 B. Arstad, H. Fjellvag, K. O. Kongshaug, O. Swang and R. Blom, *Adsorption*, 2008, **14**, 755–762.

33 S. Nandi, P. De Luna, T. D. Daff, J. Rother, M. Liu, W. Buchanan, A. I. Hawari, T. K. Woo and R. Vaidhyanathan, *Sci. Adv.*, 2015, **1**, e1500421.

34 T. A. Makal, X. Wang and H. C. Zhou, *Cryst. Growth Des.*, 2013, **13**, 4760–4768.

Electronic Supplementary Material (ESI) for Journal of Materials Chemistry A.

SI

Fine-tuning optimal porous coordination polymers by functional alkyl groups for CH_4 purification

Fujun Cheng[a]†, Qianqian Li[a]†, Jingui Duan[a,e*], Nobuhiko Hosono[b], Shin-ichiro Noro[c], Rajamani Krishna[d], Hongliang Lyu[a], Shinpei Kusaka[b], Wanqin Jin[a*] and Susumu Kitagawa[b*]

[a] State Key Laboratory of Materials-Oriented Chemical Engineering, College of Chemical Engineering, Nanjing Tech University, Nanjing 210009, China. *Email: duanjingui@njtech.edu.cn; wqjin@ njtech.edu.cn

[b] Institute for Integrated Cell-Material Sciences, Kyoto University, Yoshida, Sakyo-ku, Kyoto 606-8501, Japan. *Email: kitagawa@icems.kyoto-u.ac.jp.

[c] Research Institute for Electronic Science, Hokkaido University, Sapporo 001-0020, Japan.

[d] Van 't Hoff Institute for Molecular Sciences, University of Amsterdam, Science Park 904, 1098 XH Amsterdam, The Netherlands.

[e] Jiangsu National Synergetic Innovation Center for Advanced Materials, Nanjing Tech University, Nanjing, 210009, China.

General Procedures and Materials

All air-sensitive reactions were carried out under a dry nitrogen atmosphere using standard Schlenk techniques. All the reagents and solvents were commercially available and used as received. The FTIR spectra were recorded in the range of 4000-500 cm^{-1} on a Nicolet ID5 ATR spectrometer. Thermal analyses were performed on a Universal V3.9A TA Instruments from room temperature to 700°C with a heating rate of 10°C/min under flowing nitrogen. ^{1}H and ^{13}C NMR spectra were recorded on a Bruker 600 FT-NMR spectrometer. The powder X-ray diffraction patterns (PXRD) measurements were carried on a Bruker axs D8 Advance 40kV, 40mA for CuK_{α} (θ= 1.5418 Å) with a scan rate of 0.2 s/deg at room temperature. X-ray thermodiffractometry of as-synthesized PCPs were performed under an N_2 atmosphere from room temperature to 350℃. Simulated powder patterns from single-crystal X-ray diffraction data were generated using Mercury 1.4.2 software.

Ligand synthesis

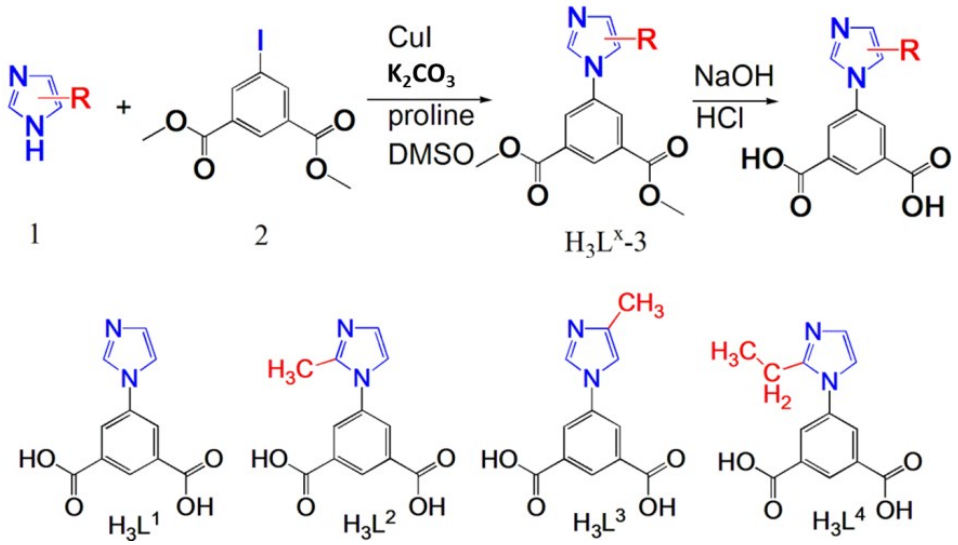

Synthesis of Compound (H_3L^1-3 Methyl ester)

Same experiment conditions, except corresponded imidazole derivatives, were used for ligands syntheses. Thus, we just describe the detail of H_3L^1 synthesis.

5-Iodo-

isophthalic acid dimethyl ester (3.6 g, 11.4 mmol), excess of imidazole (1.55 g,22.8 mmol), K_2CO_3 (3.14g,22.8mmol), CuI (0.44g 2.28mmol) and proline (0.52 g, 4.56 mmol, 0.4 equi v) were combined in dry DMSO (70 mL). The reaction system was bubbled by N_2 for 30 mins and subsequent heating at reflux for 24 hours. After the temperature cooling down, the reaction mixture was filtered. The filtrate was extracted by adding water (70 mL) and EtOAc (100 ×3 mL), dried over anhydrous $MgSO_4$, filtrated, and then concentrated. The residue was purified by silica gel column chromatography using EtOAC/Hexane (from 1:1 to 9:1) to give **H_3L^1-3** as a white solid in 62 % yield (4.80 g, 11.8 mmol).

^{1}H NMR ($CDCl_3$) of **H_3L^1-3**: 8.36 (s, 1H), 8.30 (s, 2H), 7.92 (s, 1H), 7.48 (s, 1H), 7.21 (s, 1H), 3.98 (s, 6H). ^{13}C NMR (CDCl3) of **H_3L^1-3**: 166.11, 138.83, 138.35, 136.45, 131.54, 127.72, 125.20, 118.22, 53.52.

^{1}H NMR ($CDCl_3$) of **H_3L^2-3**: 8.73 (s, 1H), 8.34 (s, 1H), 8.31 (s, 2H), 7.63 (s, 1H), 3.99 (s, 6H), 2.12 (s, 3H). ^{13}C NMR (CDCl3) of **H_3L^2-3**: 165.08, 139.69, 138.44, 136.21, 132.88, 127.79, 125.09, 115.02, 52.88, 10.66.

^{1}H NMR ($CDCl_3$) of **H_3L^3-3**: 8.36 (s, 1H), 8.36 (s, 1H), 8.34 (s, 1H), 8.31 (s, 2H), 7.63 (s, 1H), 3.97 (s, 6H), 2.42 (s, 3H). ^{13}C NMR (CDCl3) of **H_3L^2-3**: 165.05, 139.74, 138.56, 136.01, 132.95, 127.64, 125.22, 115.12, 52.37, 14.86.

^{1}H NMR ($CDCl_3$) of **H_3L^4-3**: 8.72 (s, 1H), 8.14 (s, 1H), 7.10 (s, 1H), 7.02 (s, 2H), 3.97 (s, 6H), 2.62 (q, 2H), 1.26 (t, 3H). ^{13}C NMR (CDCl3) of **H_3L^4-3**: 165.05, 149.57, 138.42, 132.27, 130.65, 130.18, 128.11, 120.46, 52.77, 20.58, 12.20.

Synthesis of H_3L^1

H_3L^1-3 (0.7 g, 2.6 mmol) was dissolved in THF (15 mL) and MeOH (15 mL). A solution of NaOH (2.1 g, 52 mmol, 20 equiv) in H_2O (30 mL) was added and the suspension heated at reflux for 10 hours upon which a clear solution was achieved. The organic solvents were evaporated and HCl (conc.) was added dropwise with stirring, precipitating the product. The flask was cooled to 0°C to ensure complete precipitation, the solids collected by filtration, washed thoroughly with water and dried at 80°C to give the desired product **H_3L^1** (0.6 g) as a white solid.

^{1}H NMR (DMSO) of **H_3L^1**: 13.61 (br s, 1.4H), 8.45 (s, 1H), 8.41 (s, 1H), 8.34 (s, 2H), 7.94 (s, 1H), 7.15 (s, 1H). ^{13}C NMR (DMSO) of **H_3L^1**: 166.36, 138.02, 136.46, 133.58, 130.71, 128.34, 125.51, 118.80.

^{1}H NMR (DMSO) of **H_3L^2**: 13.55 (br s, 0.5H), 8.56 (s, 1H), 8.25 (s, 2H), 7.73 (s, 1H), 7.41 (s, 1H), 2.43 (s, 3H). ^{13}C NMR (DMSO) of **H_3L^2**: 166.10, 145.16, 137.09, 133.57, 130.76, 130.57, 122.97, 122.57, 12.72.

^{1}H NMR (DMSO) of **H_3L^3**: 8.39 (s, 1H), 8.33 (s, 1H), 8.27 (s, 2H), 7.62 (s, 1H), 2.12 (s, 3H). ^{13}C NMR (DMSO) of **H_3L^3**: 166.65, 139.42, 138.18, 135.79, 133.96, 128.22, 124.89, 115.08, 14.15.
^{1}H NMR (DMSO) of **H_3L^4**: 8.63 (s, 1H), 8.38 (s, 2H), 7.94 (s, 1H), 7.78 (s, 1H), 2.84 (q, 2H), 1.24 (t, 3H). ^{13}C NMR (DMSO) of **H_3L^4**: 165.35, 149.11, 135.37, 133.11, 131.03, 123.09, 118.87, 55.97, 18.58, 10.80.

Single crystal X-ray studies

Single-crystal X-ray diffraction data were measured on a Bruker Smart Apex CCD diffractometer at 298 K using graphite monochromated Mo/Kα radiation (λ = 0.71073 Å). Data reduction was made with the Bruker Saint program. The cryst$_a$l of NJU-Bai3 was mounted in a flame sealed capillary containing a small amount of mother liquor to prevent desolvation during data collection, and data were collected at 298K. The structure was solved by direct methods and refined using the full-matrix least squares technique using the SHELXTL package[1]. Nonhydrogen atoms were refined with anisotropic displacement parameters during the final cycles. Organic hydrogen atoms were placed in calculated positions with isotropic displacement parameters set to 1.2Ueq of the attached atom. The unit cell includes a large region of disordered solvent molecules, which could not be modeled as discrete atomic sites. We employed PLATON/SQUEEZE[2,3] to calculate the diffraction contribution of the solvent molecules and, thereby, to produce a set of solvent-free diffraction intensities; the structure was then refined again using the data generated.

Table S1. Crystal data and structure refinement for **NTU-11** to **-14** at 298 K.

	NTU-11	**NTU-12**	**NTU-13**	**NTU-14**
Empirical formula	$C_{11}H_6CuN_2O_4$	$C_{12}H_8CuN_2O_4$	$C_{12}H_8CuN_2O_4$	$C_{13}H_{10}CuN_2O_4$
Formula weight	293.73	307.75	307.75	321.78
Crystal system	monoclinic	orthorhombic	monoclinic	monoclinic
Space group	*P21/c*	*Pbcn*	*P21/c*	*P21/c*
Unit cell dimensions	*a* = 10.830(7)Å *b* = 11.889(8)Å *c* = 14.559(9)Å *β* = 109.594(8)°	*a*= 12.678(5)Å *b*= 14.408(5)Å *c*= 20.225(7)Å	*a*= 10.915(10)Å *b*= 11.321(10)Å *c*= 14.814(12)Å *β*=109.602(13)°	*a*= 10.93(3)Å *b*= 13.71(4)Å *c*= 13.47(3)Å *β*= 111.86(3)°
Volume	1766(2) $Å^3$	3694(2) $Å^3$	1725(3) $Å^3$	1873(9) $Å^3$
Z	4	8	4	4
Density (calculated)	1.105 g/cm^3	1.107 g/cm^3	1.185 g/cm^3	1.141 g/cm^3
Mu(MoKa)	1.241 mm^{-1}	1.189 mm^{-1}	1.274 mm^{-1}	1.176 mm^{-1}
$F_{(000)}$	588	1240	620	652
Theta min-max	2.0, 25.0	2.0, 23.1	2.0, 25.0	2.2, 26.0
Index ranges	-12<=h<=12 -14<=k<=14 -16<=l<=17	-14<=h<=13 -15<=k<=15 -22<=l<=22	-11<=h<=13 -13<=k<=13 -17<=l<=17	-11<=h<=13 -16<=k<=16 -16<=l<=16
Tot., Uniq. Data, R(int)	9851,2672, 0.098	20783,2618, 0.229	11191,3042, 0.070	12914,3597, 0.154
Observed data [I > 2σ (I)]	1627	1463	2147	1575
*N*ref, *N*par	2672, 163	2618, 173	3042, 173	3597, 173
R_1, wR_2, S	0.0899, 0.2592, 1.01	0.1032, 0.2639, 1.00	0.0990, 0.3160, 1.17	0.1123, 0.3116, 1.00
Max Shift	0	0	0	0

$R = \Sigma||F_o|-|F_c||/\Sigma|F_o|$, $wR = \{\Sigma[w(|F_o|^2 - |F_c|^2)^2]/\Sigma[w(|F_o|^4)]\}^{1/2}$ and $w = 1/[\sigma^2(F_o^2) + (0.1452P)^2]$ where $P = (F_o^2+2F_c^2)/3$

Adsorption Experiments. Before the measurement, the solvent-exchanged sample was prepared by immersing the as-synthesized samples in dehydrated methanol for two days to remove the nonvolatile solvents, and the extract was decanted every 8 h and fresh acetone was replaced. The completely activated sample was obtained by heating the solvent-exchanged sample at room temperature for 6 h, 60°C for 6 h and then120°C for 24h under a dynamic high vacuum. In the gas sorption measurement, ultra-high-purity grade were used throughout the adsorption experiments. N_2 of the measured sorption isotherms have been repeated twice to confirm the reproducibility within experimental error. Gas adsorption isotherms were obtained using a Belsorpvolumetric adsorption instrument from BEL Japan Inc. using the volumetric technique.

Co-sorption measurements. Mix gas adsorptions were carried out using a multicomponent gas adsorption apparatus, Belsorp-VC (MicrotracBEL Corp.). In this apparatus, the total adsorbed amount was calculated by a constant volume method, and the composition ratio of mixed gases was determined using an Agilent 490 Micro gas chromatographic system equipped with a thermal conductive detector. From these data, we calculated adsorbed amounts and partial pressures for each gas.

Water stability experiments

For water and chemical treatment, fresh samples were soaked (around 100 mg for each) into three bottles (10 ml). HCl and NaOH were used to turn the pH of the solution to 2, 7 and 12. After one day treatment, partial samples were used for PXRD patterns collections and partial samples were used for gas sorption experiments (washed by ethanol three times and degassed at 120°C for 24h). In addition, for long term test, **NTU-14** was soaked in water at room temperature for 15 and 60 days.

Fitting of pure component isotherms

The isotherm data for H_2, CH_4, CO, CO_2, C_2H_4, and C_2H_6 in **NTU-12**, **NTU-13**, and **NTU-14** were measured at three different temperatures 273 K, 283 K, and 298 K. The data were fitted with either the single-site Langmuir or the Dual-site Langmuir model. The single-site, or dual-site Langmuir parameters are provided in Table S2, S3, S4, and S5.

$$q = q_{A,sat}\frac{b_A p}{1+b_A p} + q_{B,sat}\frac{b_B p}{1+b_B p} \qquad (1)$$

The Langmuir parameters for each site is temperature-dependent

$$b_A = b_{A0}\exp\left(\frac{E_A}{RT}\right); \quad b_b = b_{B0}\exp\left(\frac{E_B}{RT}\right); \qquad (2)$$

Table S2. *T*-dependent dual-site Langmuir parameters for CH_4, CO, CO_2, C_2H_4, and C_2H_6 in **NTU-12**.

	Site A			Site B		
	$q_{A,sat}$ mol/kg	b_{A0} Pa^{-1}	E_A kJ mol^{-1}	$q_{B,sat}$ mol/kg	b_{B0} Pa^{-1}	E_B kJ mol^{-1}
C_2H_6	4.6	7.29×10^{-12}	33	2.6	8.55×10^{-10}	29.4
C_2H_4	4	2.32×10^{-11}	30	3	3.83×10^{-10}	30
CH_4	4.6	1.36×10^{-9}	19			
CO	0.1	8.00×10^{-7}	17	3.9	1.14×10^{-9}	17
CO_2	9.4	4.85×10^{-11}	29.3	2.6	8.55×10^{-10}	29.4

Table S3. *T*-dependent dual-site Langmuir parameters for CH_4, CO, CO_2, C_2H_4, and C_2H_6 in **NTU-13**.

	Site A			Site B		
	$q_{A,sat}$ mol/kg	b_{A0} Pa^{-1}	E_A kJ mol^{-1}	$q_{B,sat}$ mol/kg	b_{B0} Pa^{-1}	E_B kJ mol^{-1}
C_2H_6	0.8	8.85×10^{-12}	33	3	9.76×10^{-11}	36.7
C_2H_4	0.7	1.96×10^{-11}	31.6	3	7.43×10^{-11}	36.3
CH_4	3	4.61×10^{-10}	24.5			
CO	0.08	7.04×10^{-8}	21.6	4.5	2.33×10^{-10}	21.6
CO_2	3.5	1.64×10^{-11}	30	2.8	7.13×10^{-11}	34.8

Table S4. *T*-dependent dual-site Langmuir parameters for CH_4, CO, CO_2, C_2H_4, and C_2H_6 in **NTU-14**.

	Site A			Site B		
	$q_{A,sat}$ mol/kg	b_{A0} Pa^{-1}	E_A kJ mol^{-1}	$q_{B,sat}$ mol/kg	b_{B0} Pa^{-1}	E_B kJ mol^{-1}
C_2H_6	3.1	2.19×10^{-11}	37.3			
C_2H_4	3.2	5.55×10^{-11}	34.4			

CH_4	3.2	7.24×10^{-10}	21.3			
CO	0.025	1.12×10^{-6}	18.6	2.4	8.58×10^{-10}	18.6
CO_2	4.8	6.34×10^{-11}	30			

Table S5. Langmuir parameters for H_2 at 298 K in **NTU-12**, **NTU-13**, and **NTU-14**.

	$q_{A,sat}$ mol/kg	b_A Pa^{-1}
NTU-12	4	7.91×10^{-8}
NTU-13	5	4.37×10^{-8}
NTU-14	5	6.00×10^{-8}

Isosteric heat of adsorption

The binding energies of CH_4, CO, CO_2, C_2H_4, and C_2H_6 in **NTU-12**, **NTU-13**, and **NTU-14** are reflected in the isosteric heat of adsorption, Q_{st}, defined as

$$Q_{st} = RT^2\left(\frac{\partial \ln p}{\partial T}\right)_q \qquad (3)$$

These values were determined using the pure component isotherm fits.

The adsorption selectivities of the three binary pairs C_2H_4/CH_4, C_2H_4/CO, and C_2H_4/H_2 can be determined from

$$S_{ads} = \frac{q_i/q_j}{p_i/p_j} \qquad (4)$$

In equation (4), q_i, and q_j are the molar loadings in the adsorbed phase in equilibrium with the bulk gas phase with partial pressures p_i, and p_j.

Transient breakthrough of mixtures in fixed bed adsorbers

The performance of industrial fixed bed adsorbers is dictated by a combination of adsorption selectivity and uptake capacity. For a proper comparison of **NTU-12**, **NTU-13**, and **NTU-14**, we perform transient breakthrough simulations using the simulation methodology described in the literature[4-6]. For the breakthrough simulations, the following parameter values were used: length of packed bed, L = 0.3 m; voidage of packed bed, □ = 0.4; superficial gas velocity at inlet, u = 0.04 m/s. The transient breakthrough simulation results are presented in terms of a *dimensionless* time, ε, defined by dividing the actual time, t, by the characteristic time, $\frac{L\varepsilon}{u}$.

Structures of NTU-11 to -14

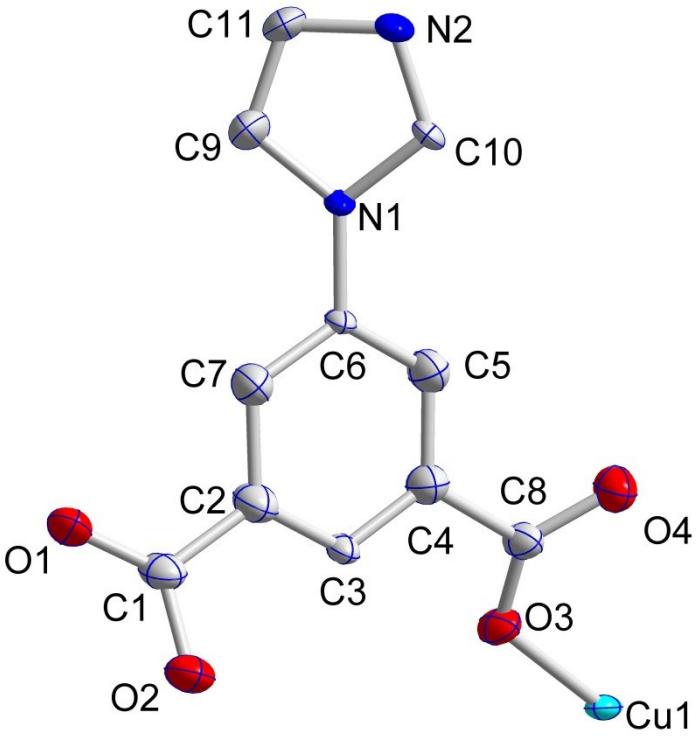

Fig. S1 View of asymmetric unit of **NTU-11**.

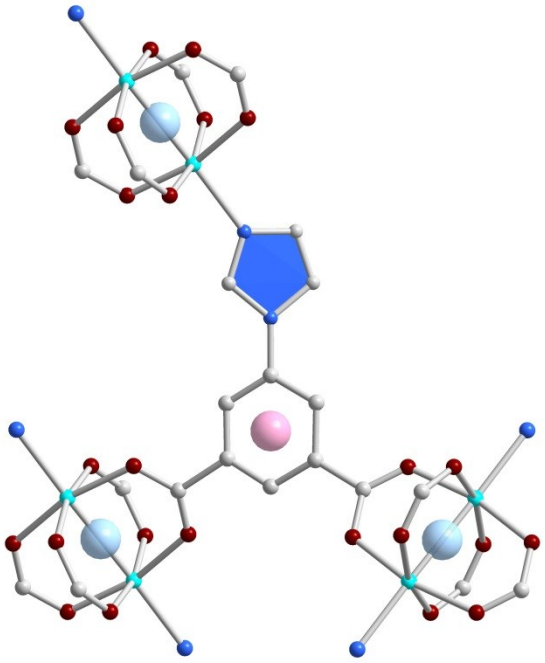

Fig. S2 View of ligand connection of **NTU-11**.

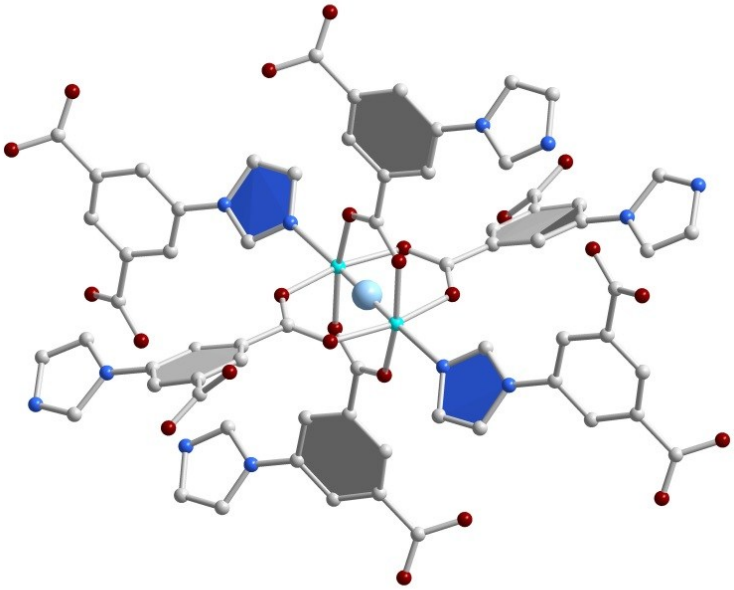

Fig. S3 View of cluster connection of **NTU-11**.

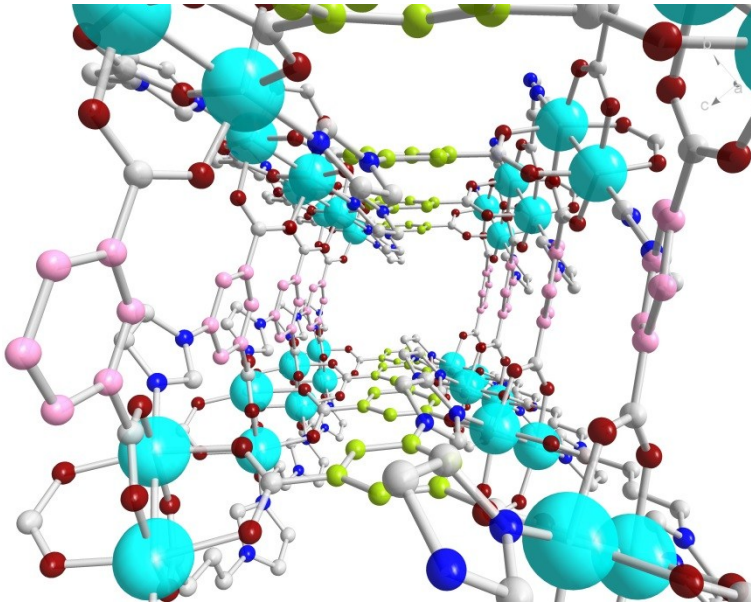

Fig. S4 View of 1D channel in **NTU-11** along c-axis.

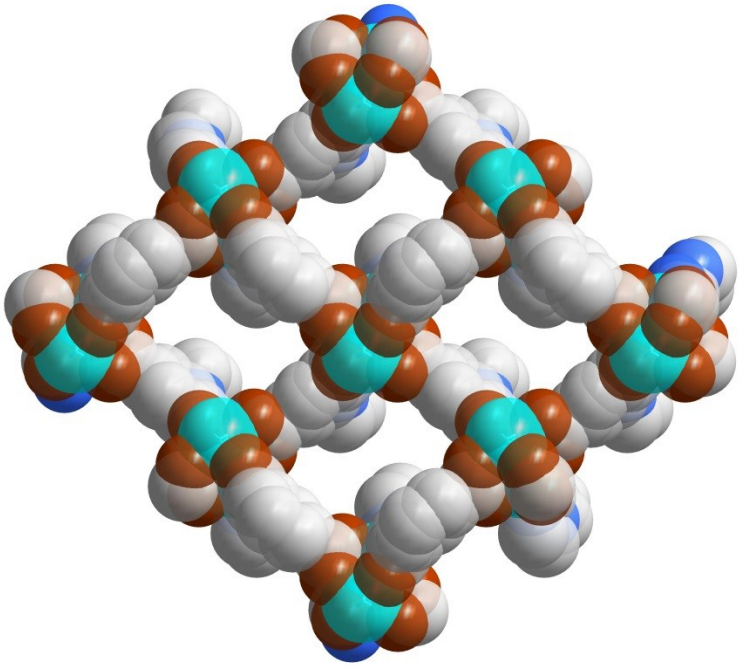

Fig. S5 View of crystal packing along c-axis in **NTU-11**.

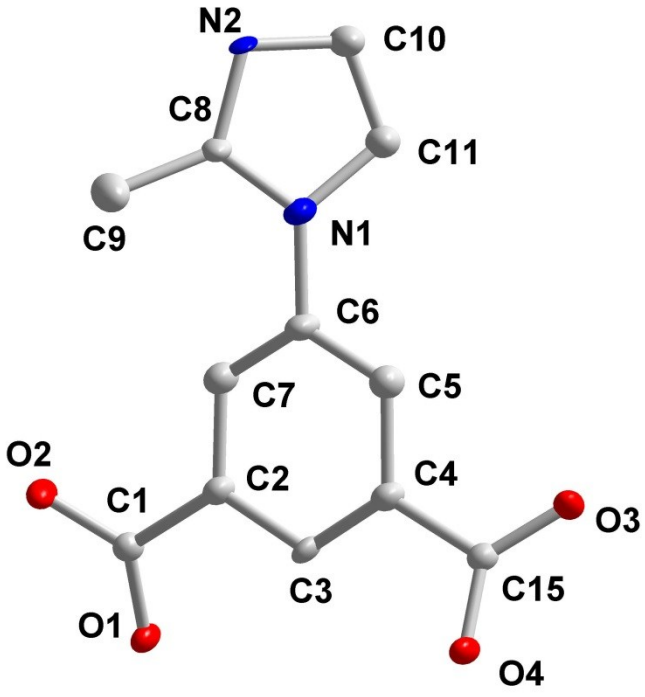

Fig. S6 View of asymmetric unit of **NTU-12**.

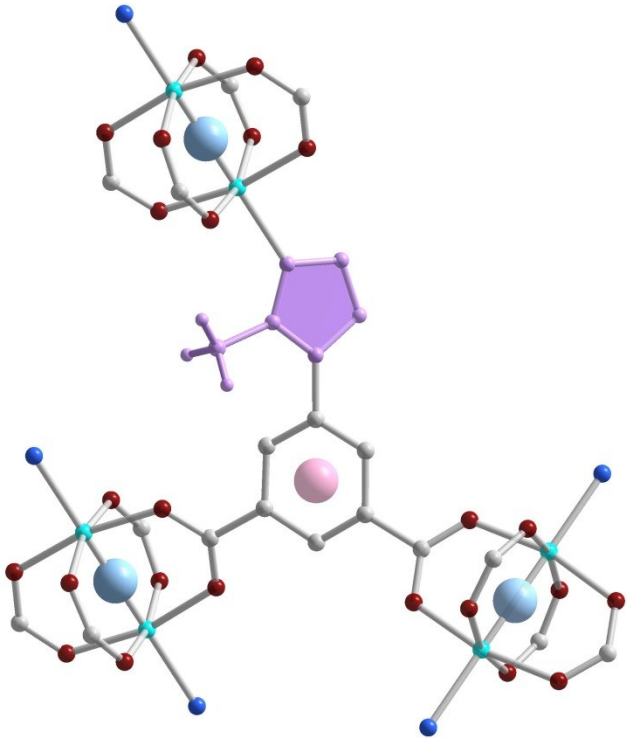

Fig. S7 View of ligand connection in **NTU-12**.

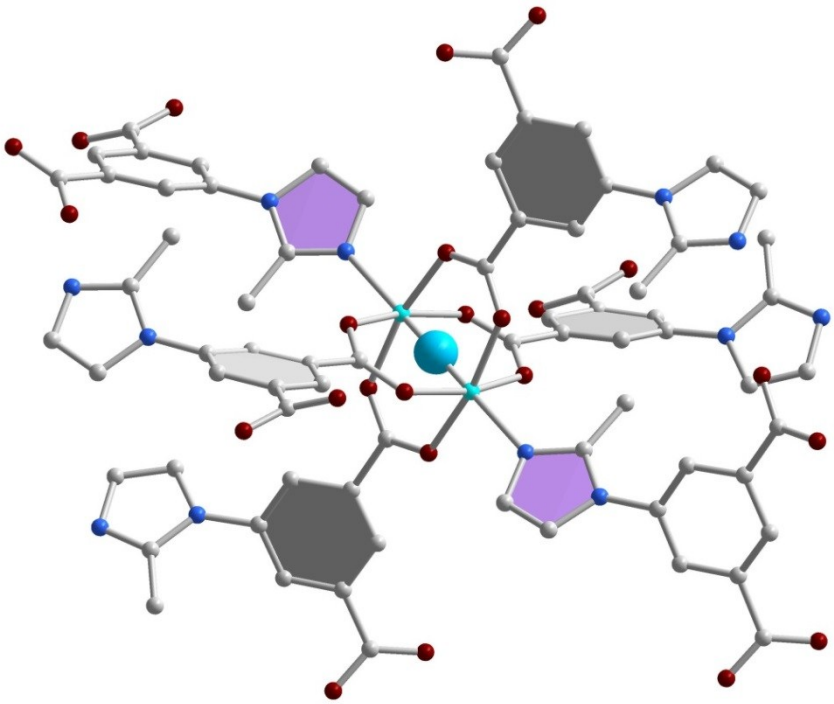

Fig. S8 View of cluster connection in **NTU-12**.

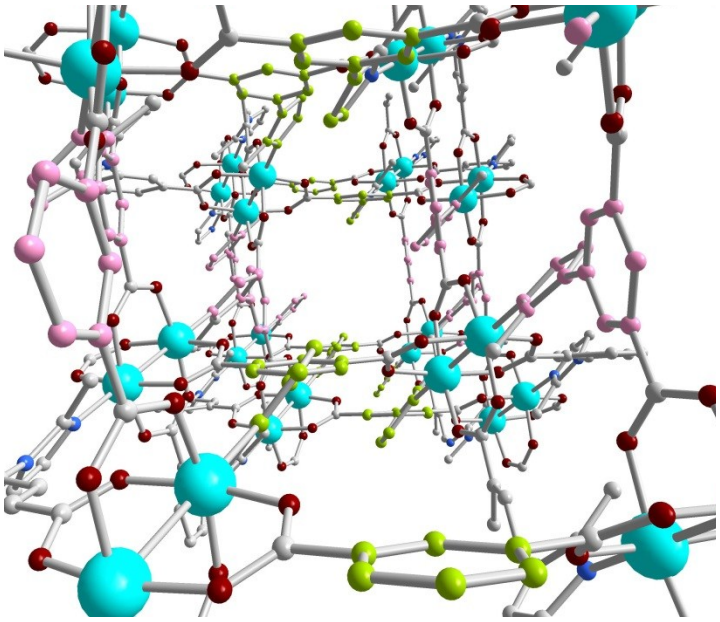

Fig. S9 View of 1D channel in **NTU-12** along c-axis.

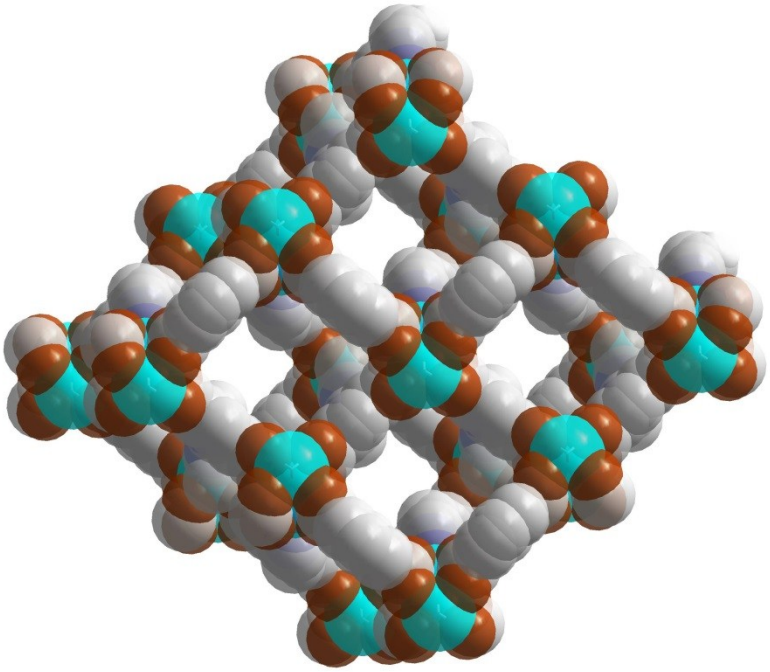

Fig. S10 View of crystal packing along c-axis in **NTU-12**.

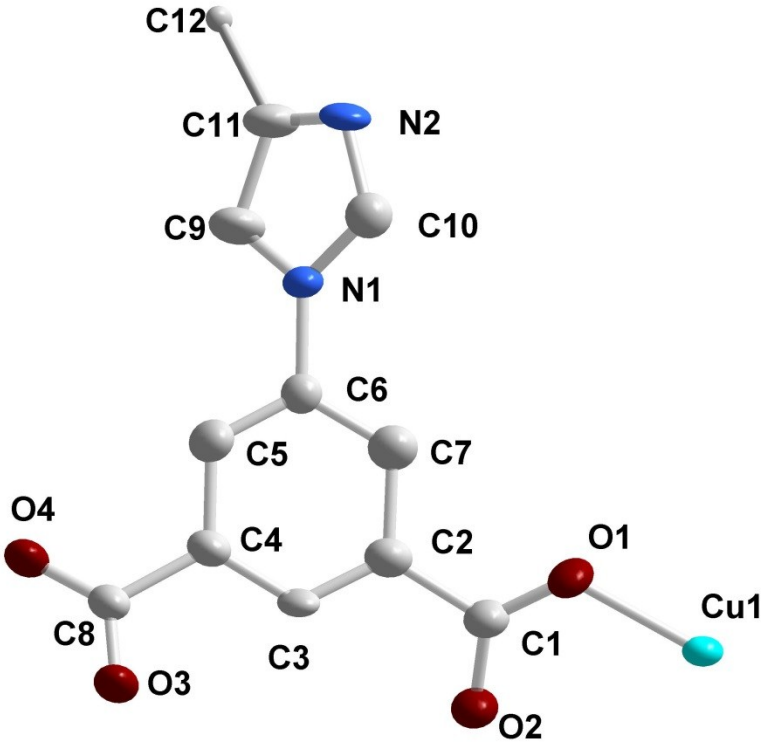

Fig. S11 View of asymmetric unit of **NTU-13**.

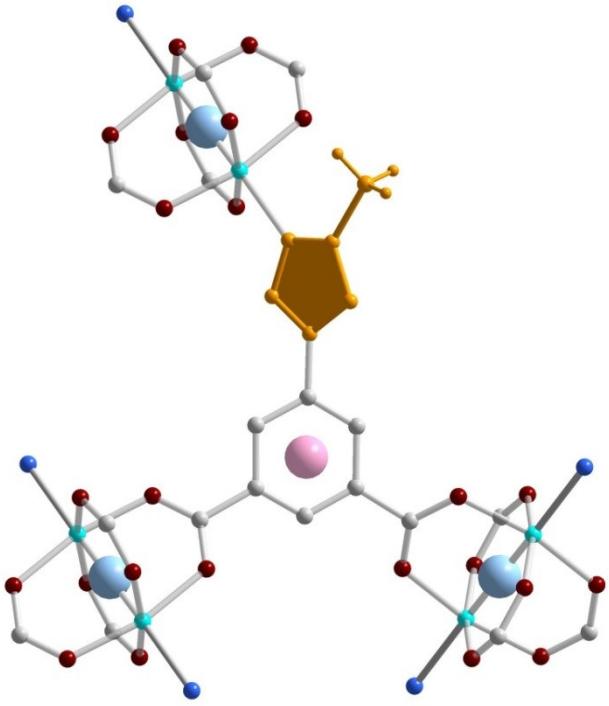

Fig. S12 View of ligand connection in **NTU-13**.

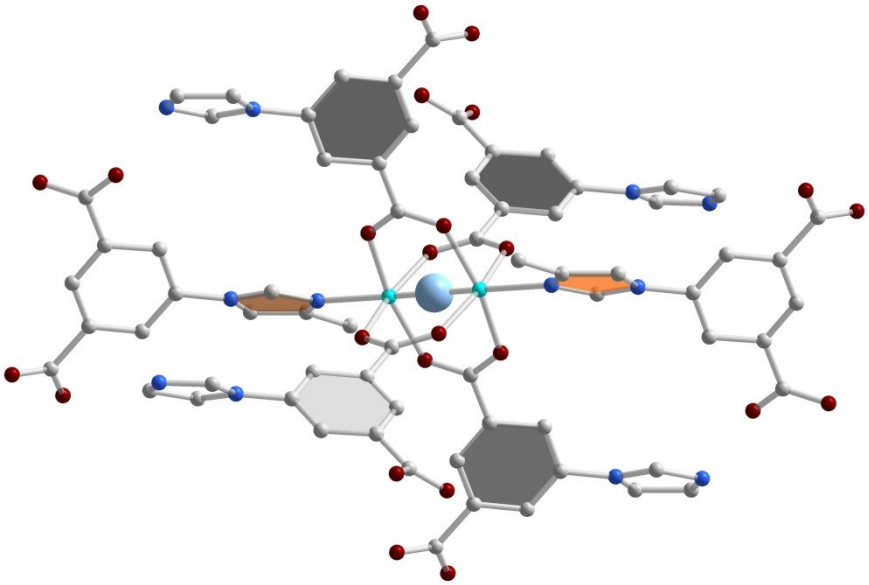

Fig. S13 View of cluster connection in **NTU-13**.

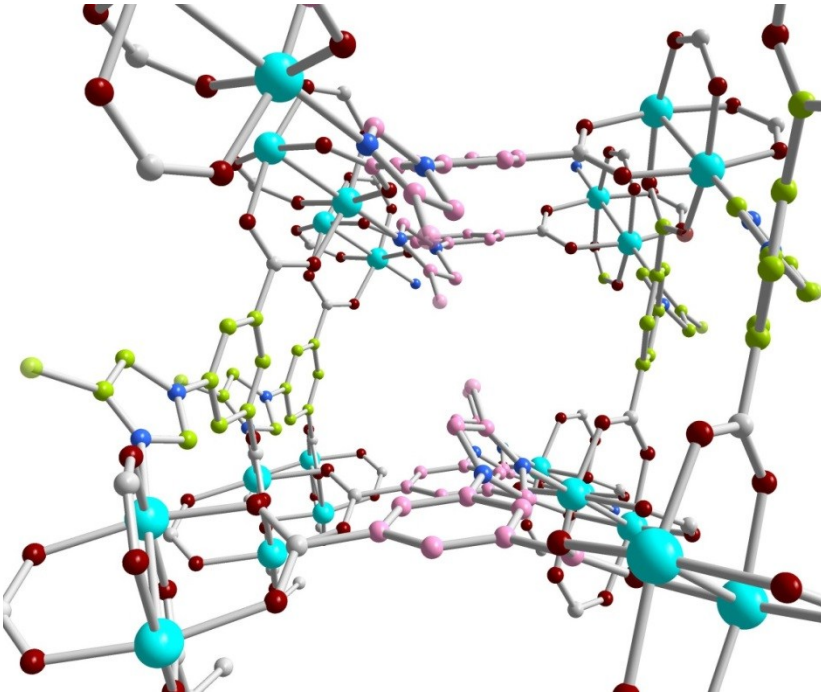

Fig. S14 View of 1D channel in **NTU-13** along c-axis.

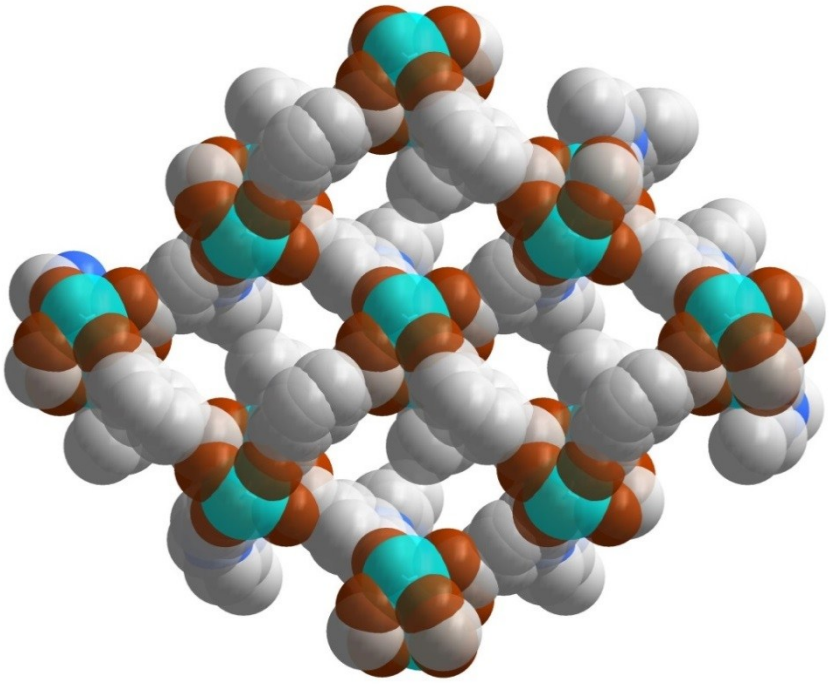

Fig. S15 View of crystal packing along c-axis in **NTU-13**.

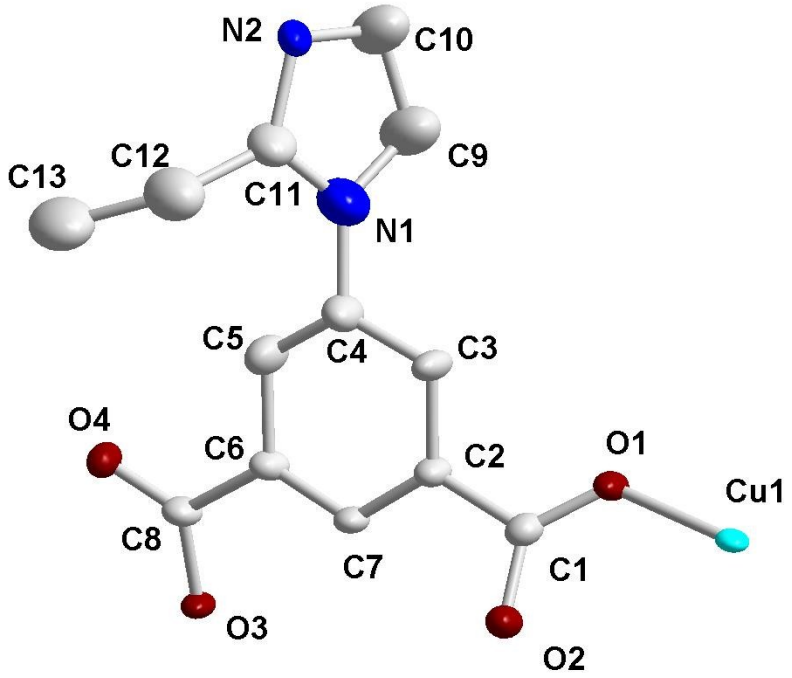

Fig. S16 View of asymmetric unit of **NTU-14**.

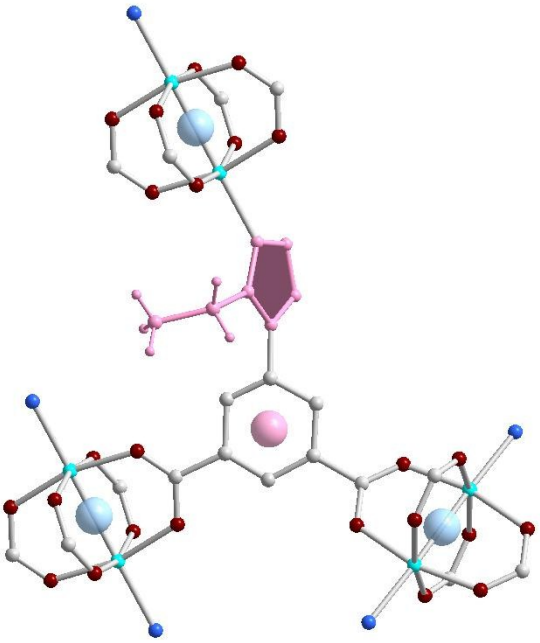

Fig. S17 View of ligand connection in **NTU-14**.

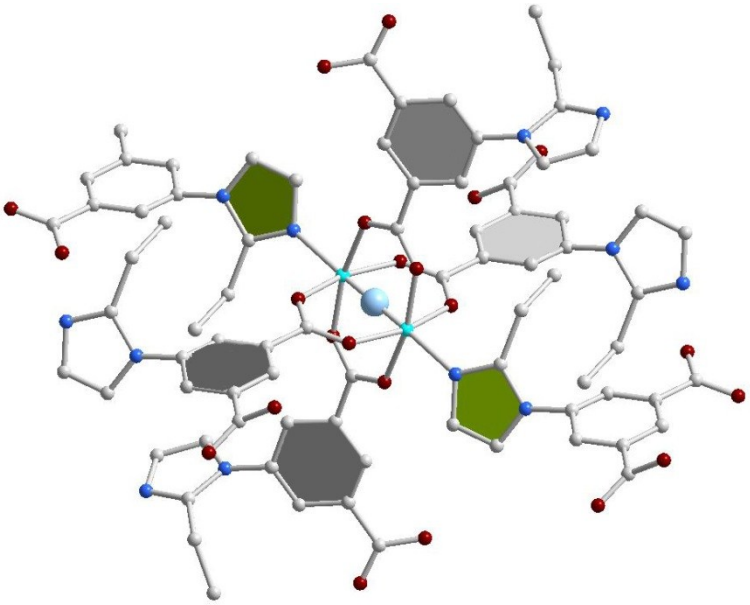

Fig. S18 View of cluster connection in **NTU-14**.

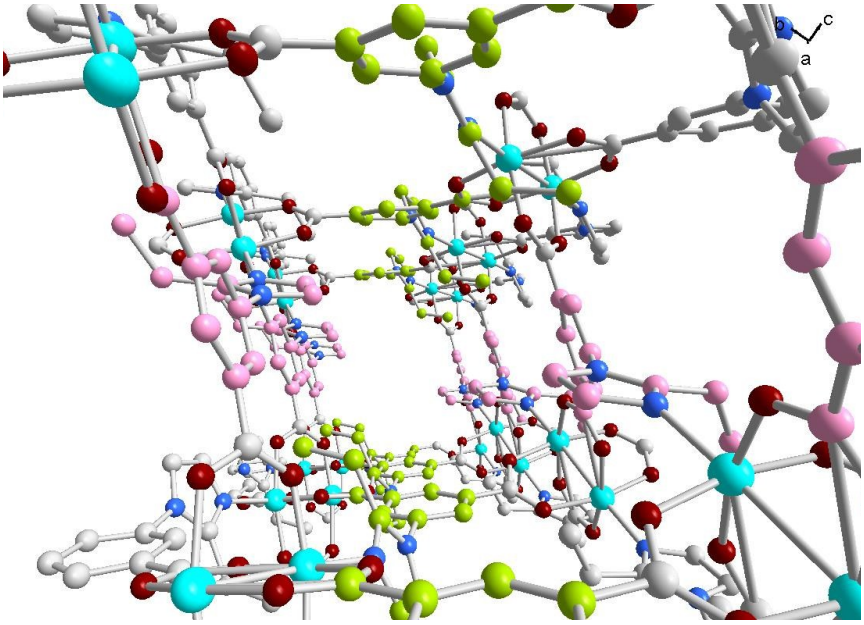

Fig. S19 View of 1D channel in **NTU-14** along c-axis.

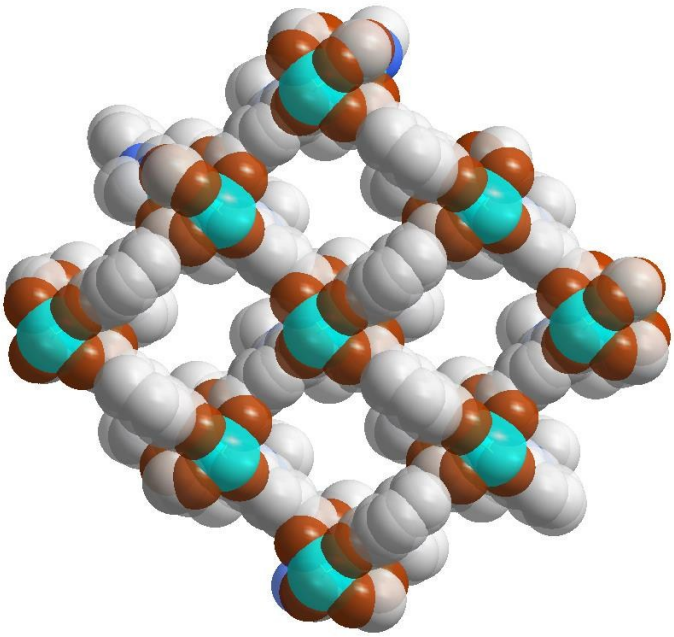

Fig. S20 View of crystal packing along c-axis in **NTU-14**.

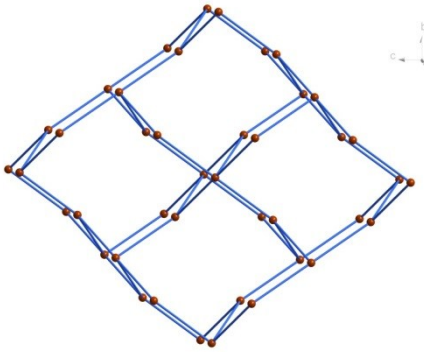

3,6-c apo/alpha topology of **NTU-11**

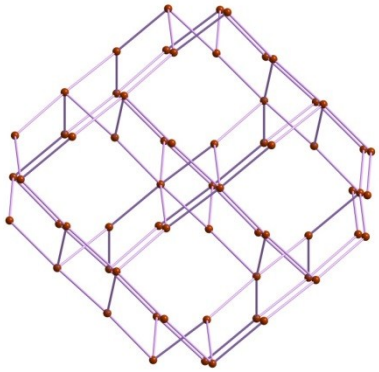

3,6-c apo/alpha topology of **NTU-12**

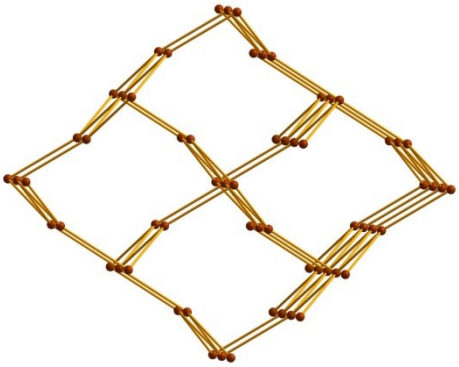

3,6-c apo/alpha topology of **NTU-13**

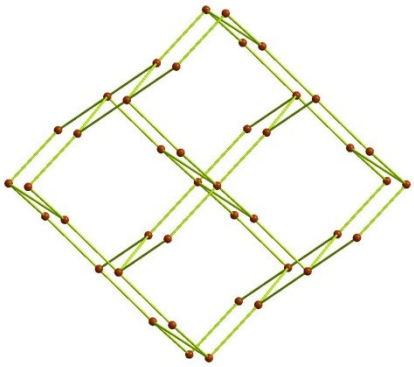

3,6-c apo/alpha topology of **NTU-14**

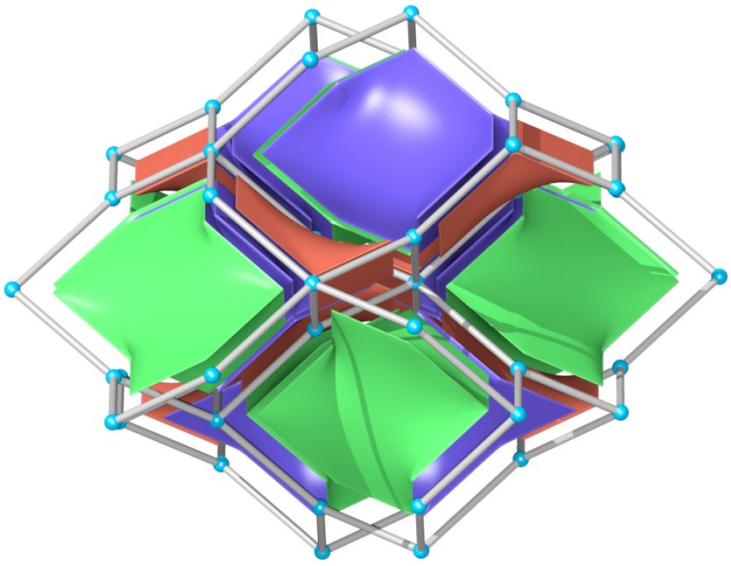

Tiles of apo/alpha net

Fig. S21 Topology comparison and tiles of **NTU-11** to **-14**.

Structural characterizations

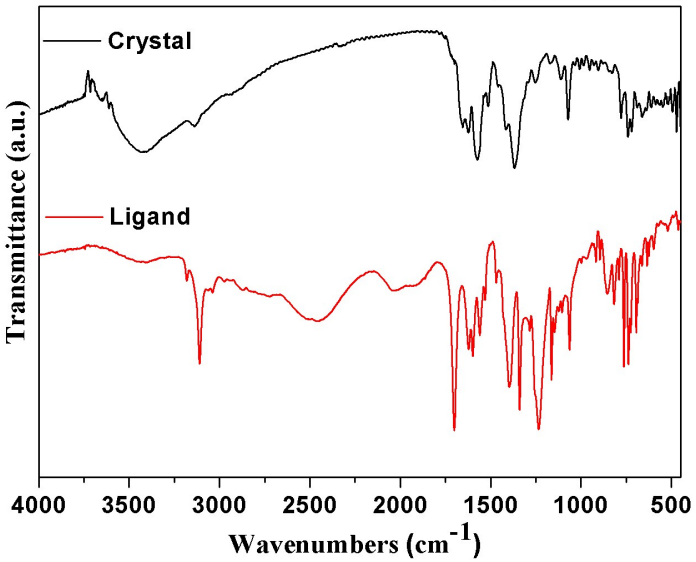

Fig. S22 IR of as-synthesized crystal of **NTU-11** and **H_3L^1** ligand.

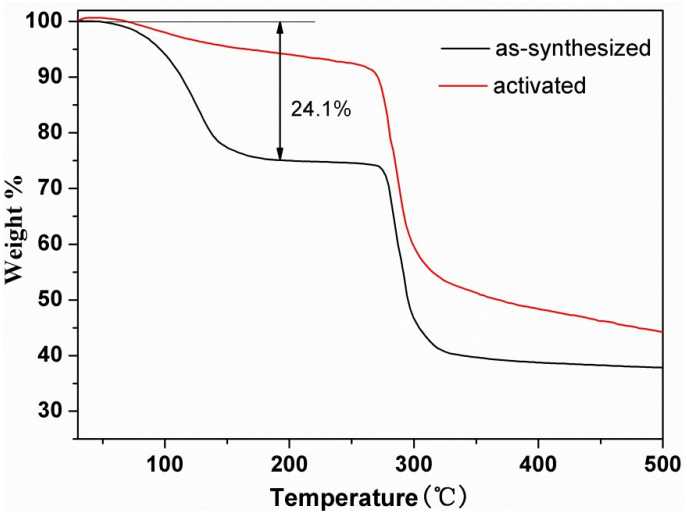

Fig. S23 TG of as-synthesized and activated **NTU-11**. The weight loss before 100 °C of activated sample should be assigned as the quick moisture adsorption in air during sample loading. Combine the squeezed electronic, the solvent inside the channel can be evaluated. The electronic number of H_2O is 10, while the electronic number of DMF is 40. Therefore: Number of electronics: (10+40) × 4 = 200 (found: 197); TG weight loss: (18+73)/[(18+73)+293.7] = 23.6% (found: 24.1%).

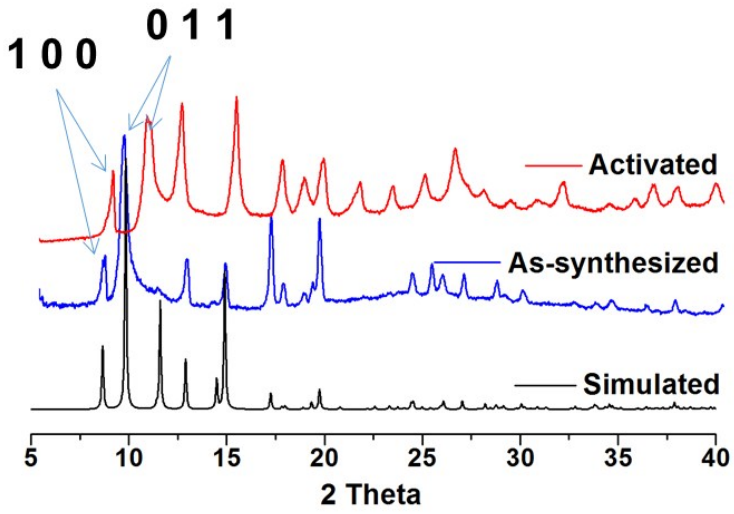

Fig. S24 PXRD of simulated and as-synthesized **NTU-11**.

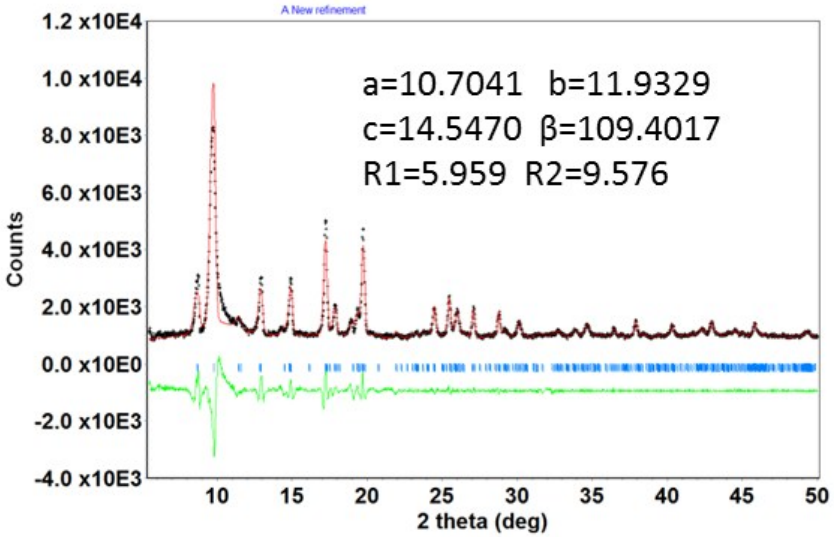

Fig. S25 The results of Le Bail analysis for the PXRD of **NTU-11**. Refined parameters and reliability factors are close to the data that derived from single crystal analysis.

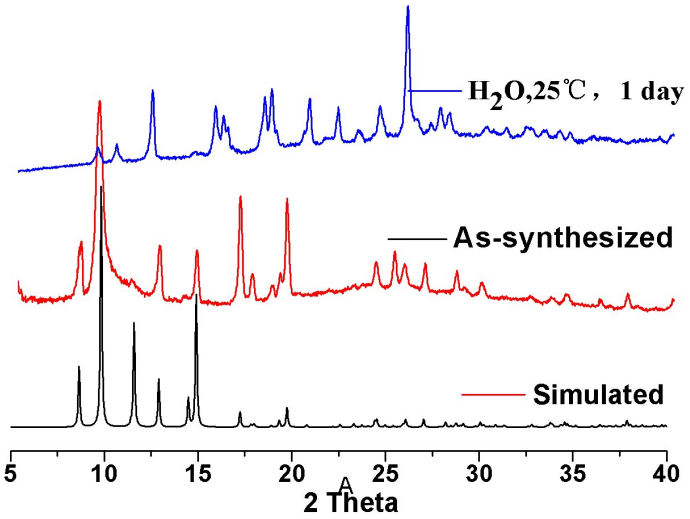

Fig. S26 PXRD results of water treated and fresh crystal of **NTU-11**. Shifted position of some peaks indicates weak water stability.

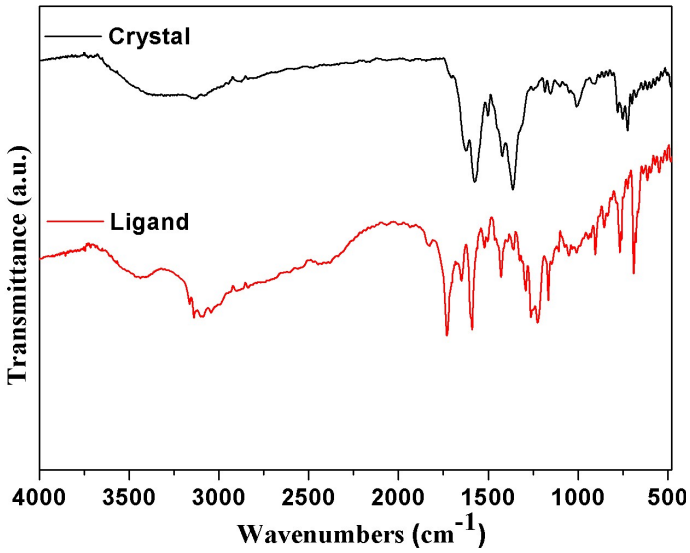

Fig. S27 IR of as-synthesized **NTU-12** and **H_3L^2** ligand.

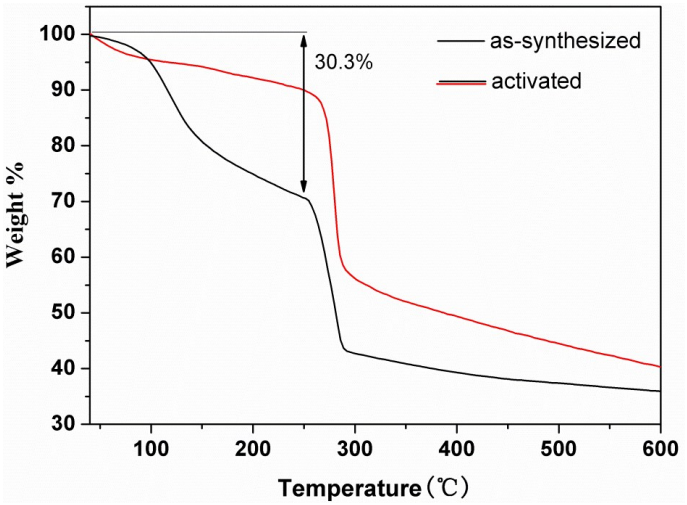

Fig. S28 TG of as-synthesized and activated **NTU-12**. The weight loss before 100 °C of activated sample should be assigned as the quick moisture adsorption in air during sample loading. Combine the squeezed electronic, the solvent inside the channel can be evaluated. The electronic number of H_2O is 10, while the electronic number of DMF is 40. Therefore: Number of electronics: (10×1.5+40×1.5) × 8 = 600 (found: 609); TG weight loss: (1.5×18+1.5×73)/ [(1.5×18+1.5×73)+307.75] = 30.7% (found: 30.3%).

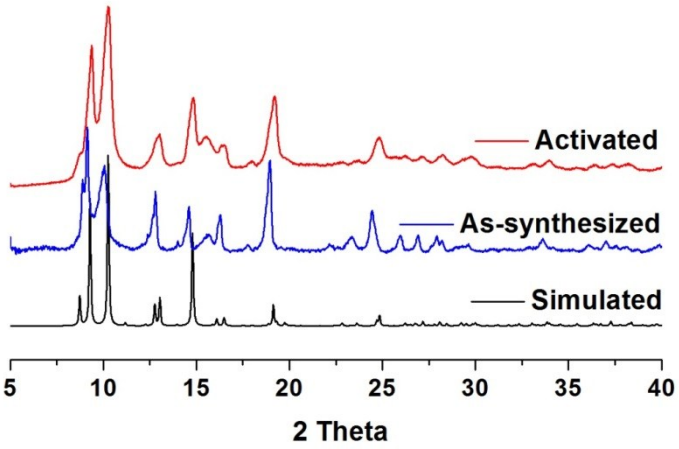

Fig. S29 PXRD of simulated, as-synthesized and activated **NTU-12**.

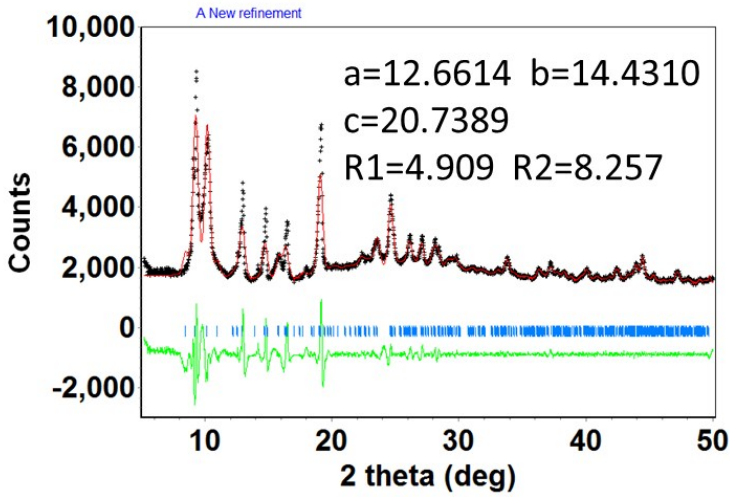

Fig. S30 The results of Le Bail analysis for the PXRD of **NTU-12**. Refined parameters and reliability factors are close to the data that derived from single crystal analysis.

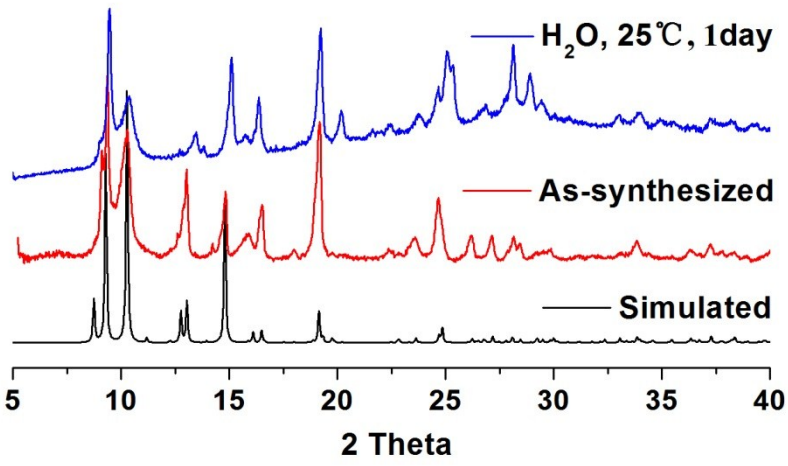

Fig. S31 PXRD results of water treated and fresh crystal of **NTU-12**.

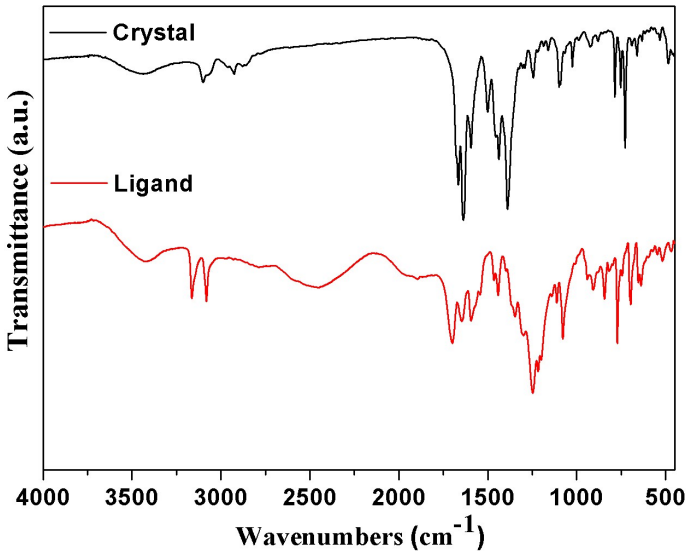

Fig. S32 IR of as-synthesized crystal of **NTU-13** and **H_3L^3** ligand.

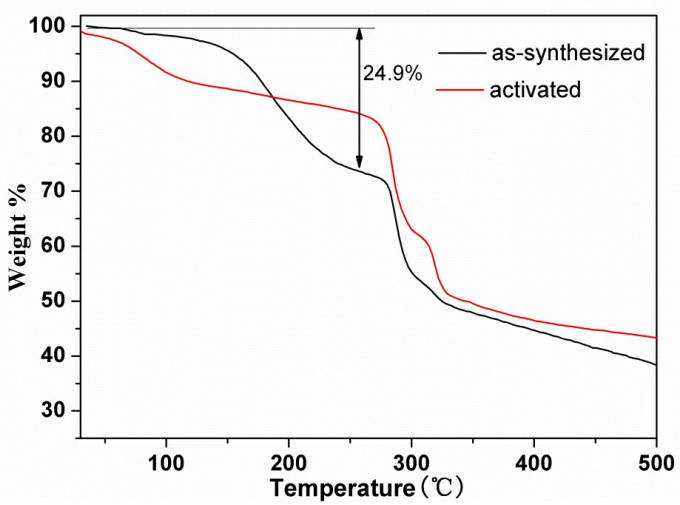

Fig. S33 TG of as-synthesized and activated **NTU-13**. The weight loss before 100 °C of activated sample should be assigned as the quick moisture adsorption in air during sample loading. ombine the squeezed electronic, the solvent inside the channel can be evaluated. The electronic number of H_2O is 10, while the electronic number of DMF is 40. Therefore: Number of electronics: (10×1.5+40) × 4 = 220 (found: 221); TG weight loss: (1.5×18+73)/[(1.5×18+73)+307.7] = 24.5% (found: 24.9%).

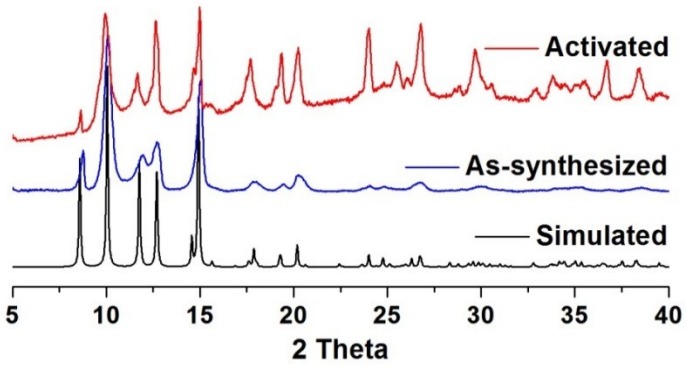

Fig. S34 PXRD of simulated, as-synthesized and activated **NTU-13**.

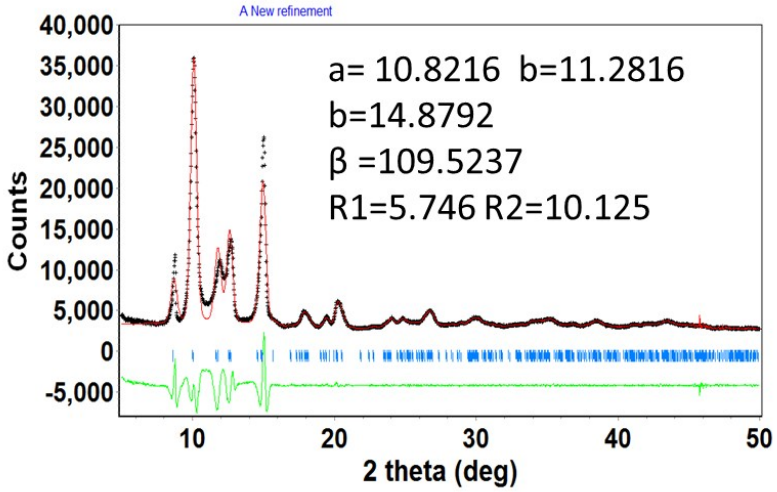

Fig. S35 The results of Le Bail analysis for the PXRD of **NTU-13**. Refined parameters and reliability factors are close to the data that derived from single crystal analysis.

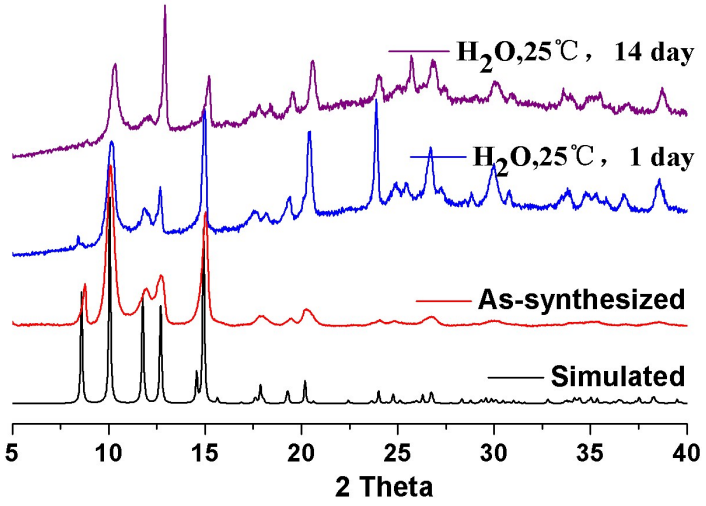

Fig. S36 PXRD results of water treated and fresh crystal of **NTU-13**.

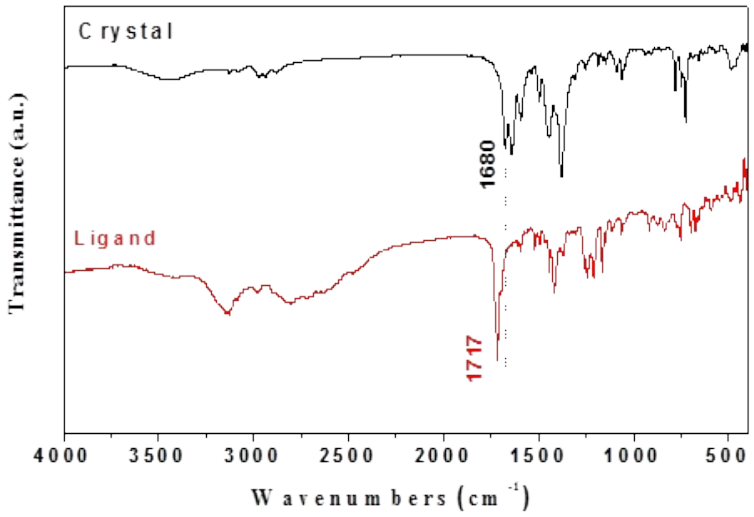

Fig. S37 IR of as-synthesized crystal of **NTU-14** and **H_3L^4** ligand.

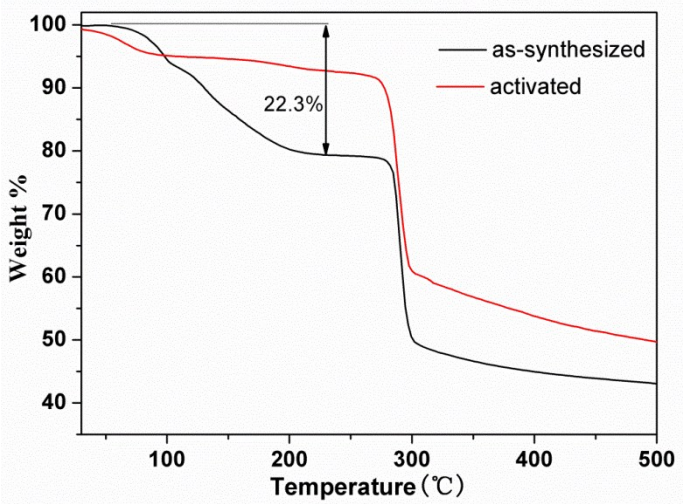

Fig. S38 TG of as-synthesized and activated **NTU-14**. The weight loss before 80 °C of activated sample should be assigned as the quick moisture adsorption in air during sample loading. Combine the squeezed electronic, the solvent inside the channel can be evaluated. The electronic number of H_2O is 10, while the electronic number of DMF is 40. Therefore: Number of electronics: (10×1.2+40) × 4 = 210 (found: 209); TG weight loss: (1.2×18+73)/ [(1.2×18+73)+321.7] = 22.7% (found: 22.3%).

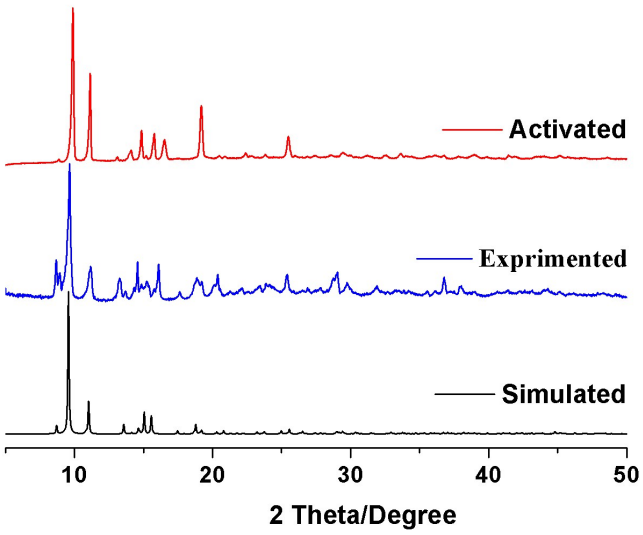

Fig. S39 PXRD of simulated, as-synthesized and activated **NTU-14**.

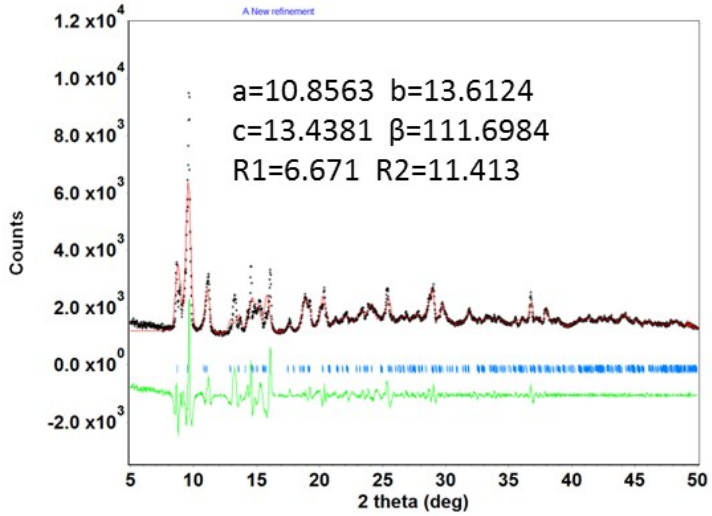

Fig. S40 The results of Le Bail analysis for the PXRD of **NTU-14**. Refined parameters and reliability factors are close to the data that derived from single crystal analysis.

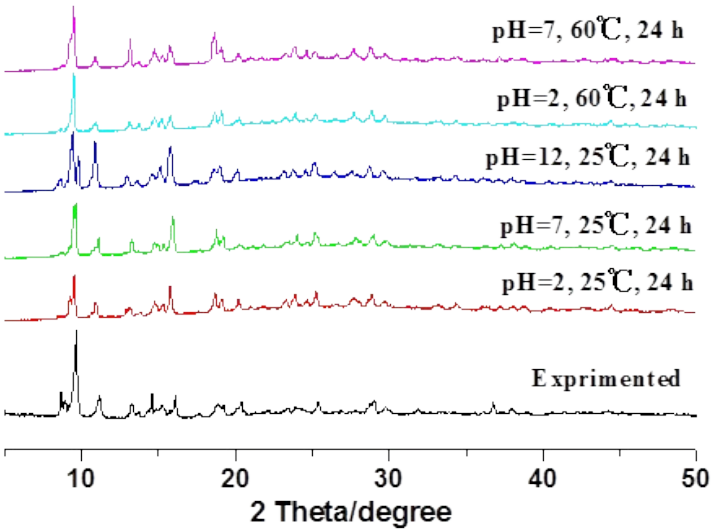

Fig. S41 PXRD of water and chemical treated **NTU-14**.

Adsorption isotherms

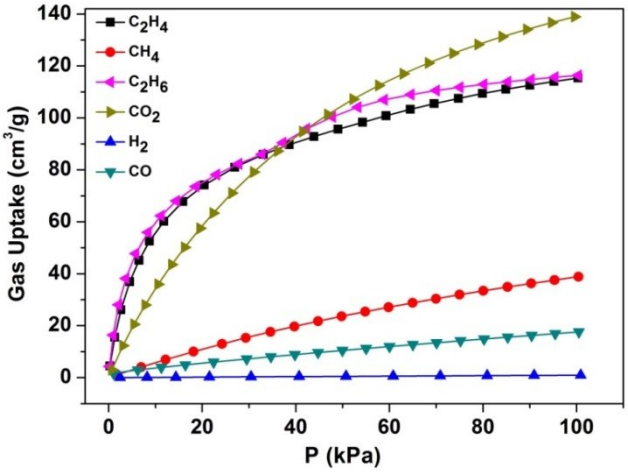

Fig. S42 Gas adsorption of **NTU-12** at 273 K.

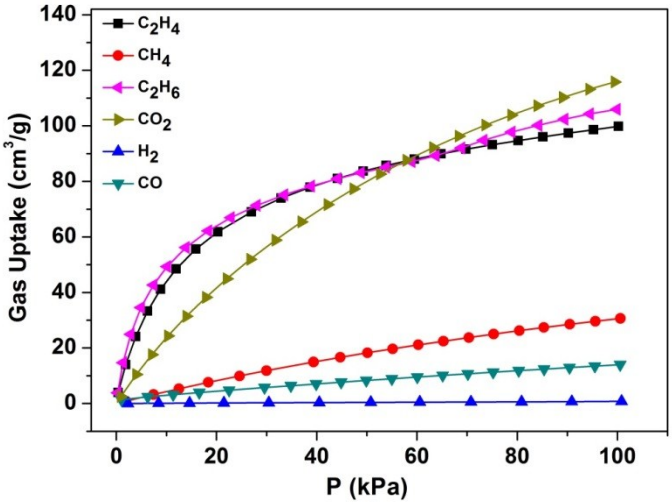

Fig. S43 Gas adsorption of **NTU-12** at 283 K.

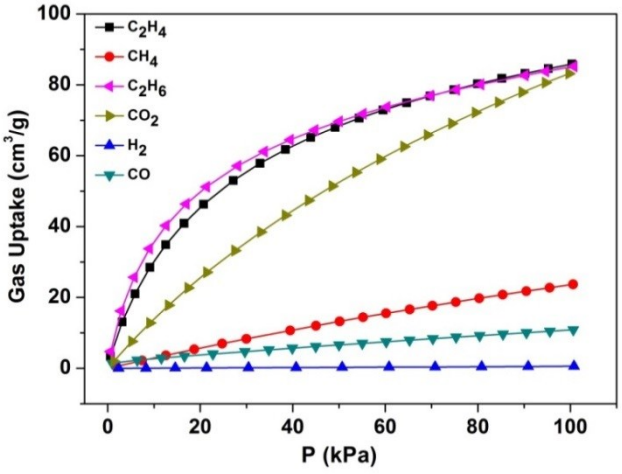

Fig. S44 Gas adsorption of **NTU-12** at 298 K.

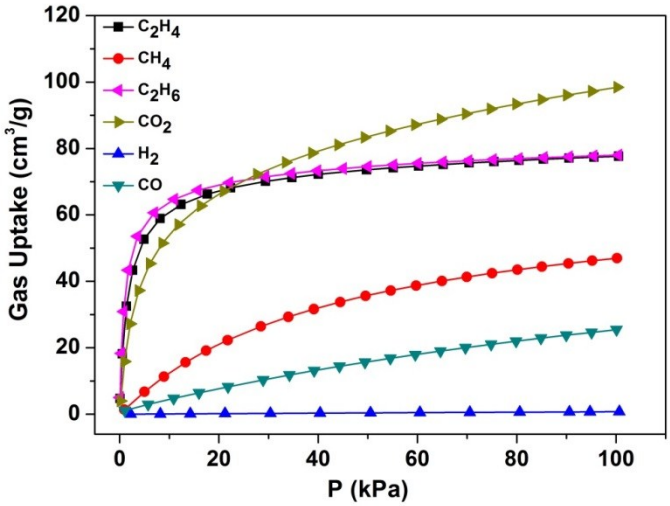

Fig. S45 Gas adsorption of **NTU-13** at 273 K.

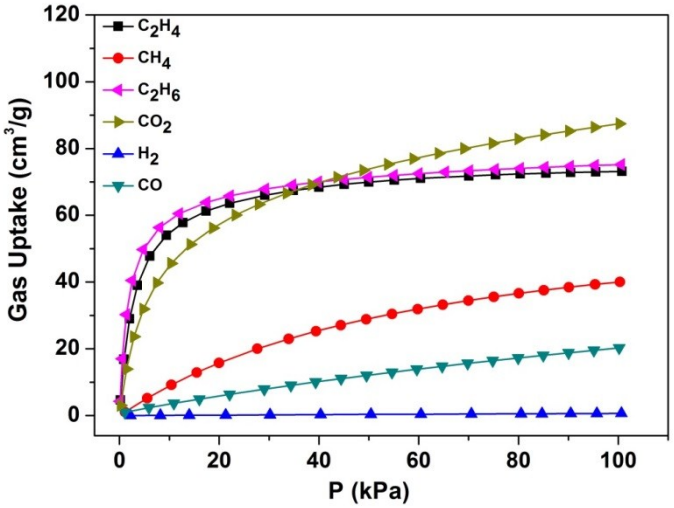

Fig. S46 Gas adsorption of **NTU-13** at 283 K.

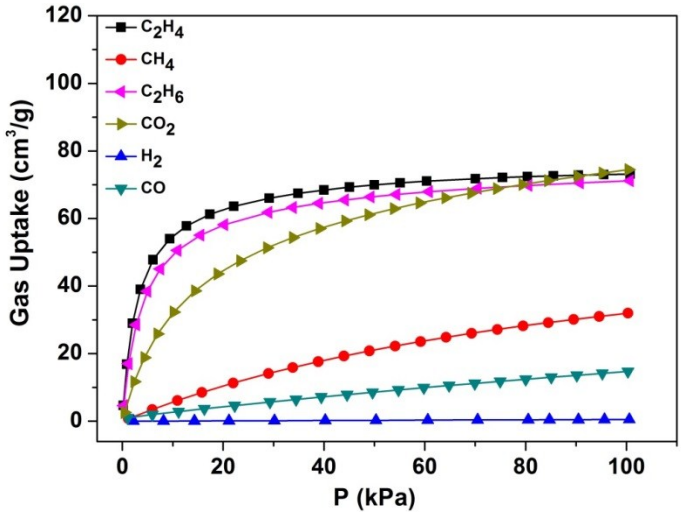

Fig. S47 Gas adsorption of **NTU-13** at 298 K.

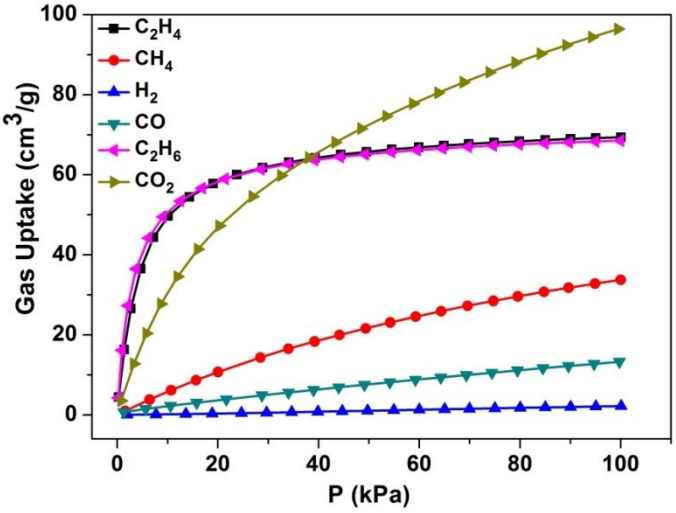

Fig. S48 Gas adsorption of **NTU-14** at 273 K.

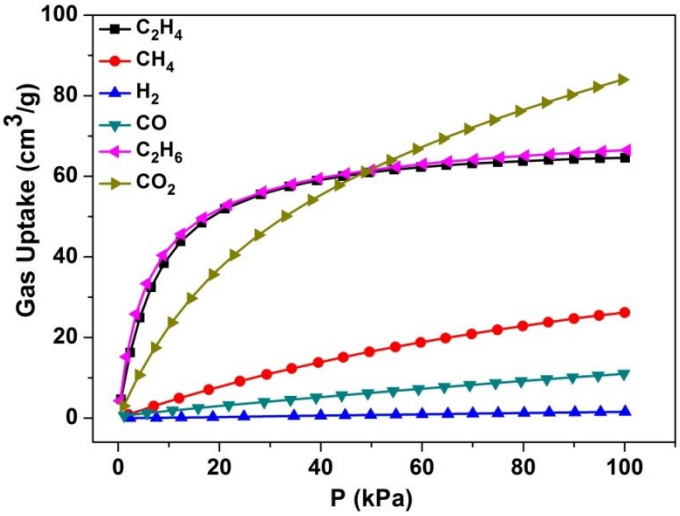

Fig. S49 Gas adsorption of **NTU-14** at 283 K.

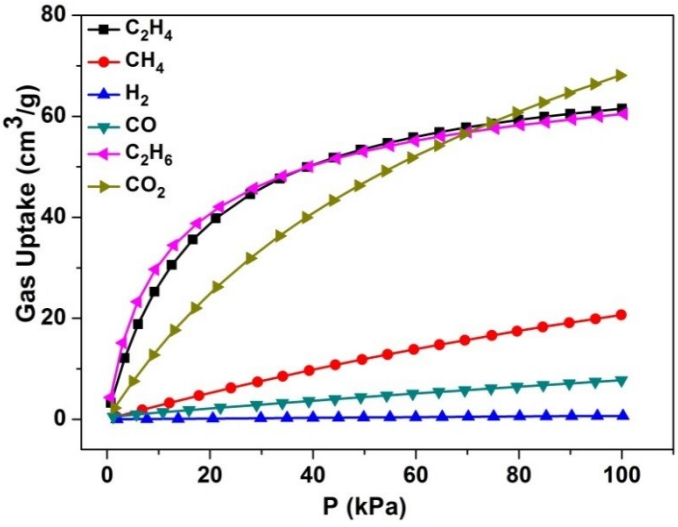

Fig. S50 Gas adsorption of **NTU-14** at 298 K.

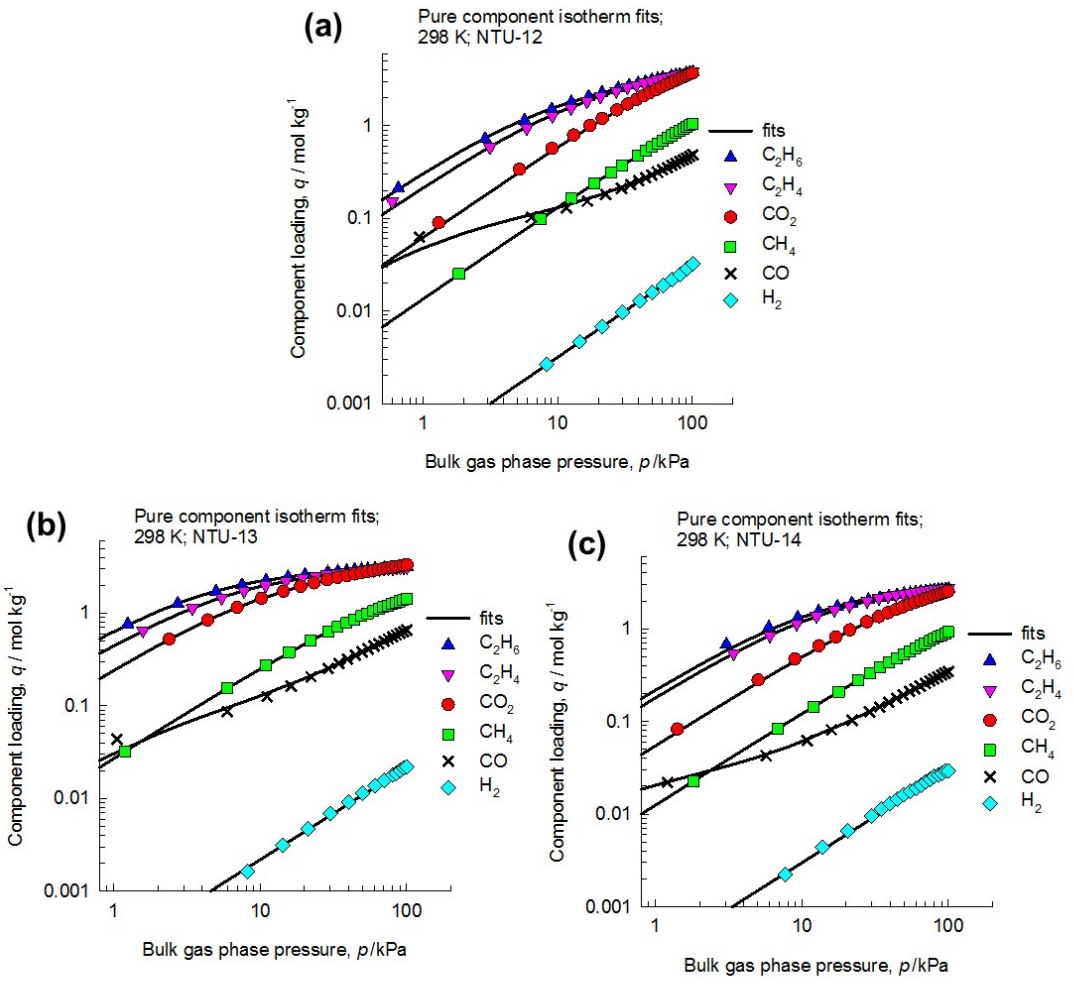

Fig. S51 Comparison of experimental data on component loadings for H_2, CH_4, CO, CO_2, C_2H_4, and C_2H_6 at 298 K in (a) **NTU-12**, (b) **NTU-13**, and (c) **NTU-14** at 298 K with the isotherm fits.

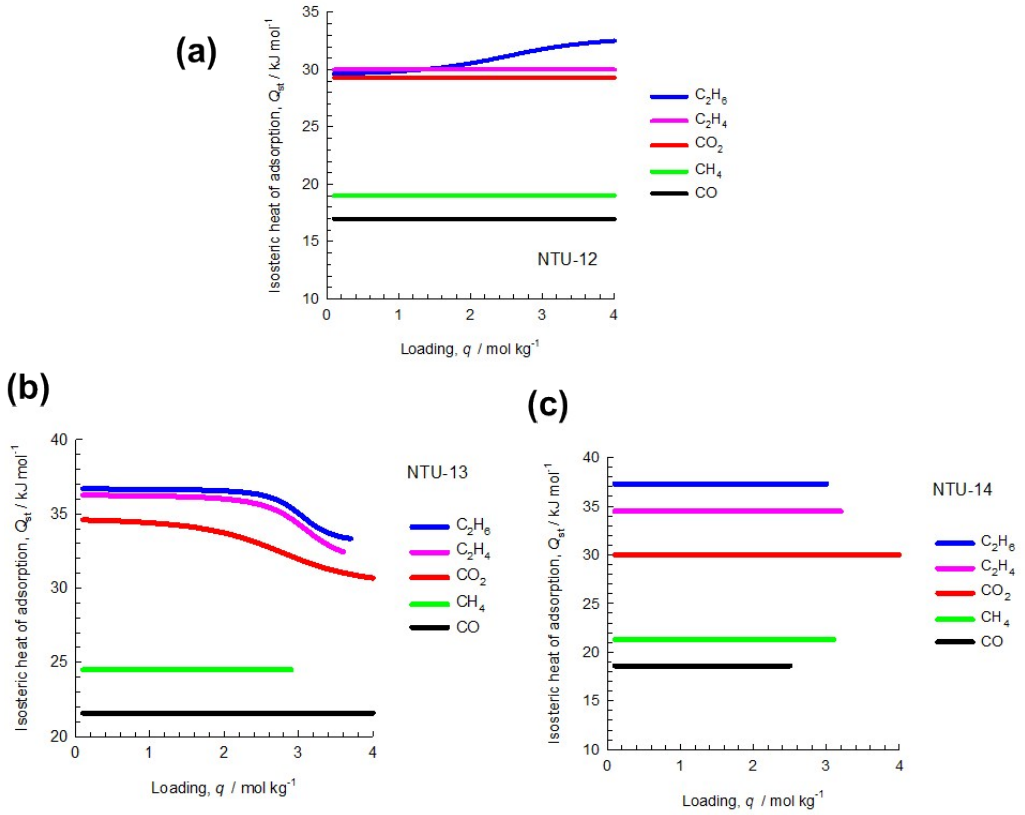

Fig. S52 The isosteric heat of adsorption, Q_{st}, for CH_4, CO, CO_2, C_2H_4, and C_2H_6 at 298 K in (a) **NTU-12**, (b) **NTU-13**, and (c) **NTU-14** at 298 K**.** The determination of the Q_{st} is based on the Clausius-Clapeyron equation.

Table S6. Calculated gas selectivity in **NTU-12**, **-13** and **-14** by IAST model at 298K, 1bar.

	C_2H_4/CH_4	CO_2/CH_4	C_2H_4/CO	CO_2/CO	C_2H_4/H_2
NTU-12	14.7	5.6	40.3	13.2	688.8
NTU-13	20.4	10.5	44.4	26.3	1391.8
NTU-14	15.2	6.9	60.9	23.8	472.5

From this table, we note that the selectivity of CO_2/CO in **NTU-12** (13.2) was improved 2 times in **NTU-13** (26.29) and 1.8 times in **NTU-14** (23.8). In addition, the selectivity of C_2H_4/CH_4 also shows obvious improvement in **NTU-13** (20.4) and **-14** (15.2), indicating high practical feasibility of C1/C2 hydrocarbon separation. Meanwhile, due to low H_2 uptake, the C_2H_4/H_2 selectivity in them was predicted to be extremely high. Therefore, the inherent gas selectivities for those three PCPs appear to be dictated by host-guest interactions, and also polarizability of molecules.

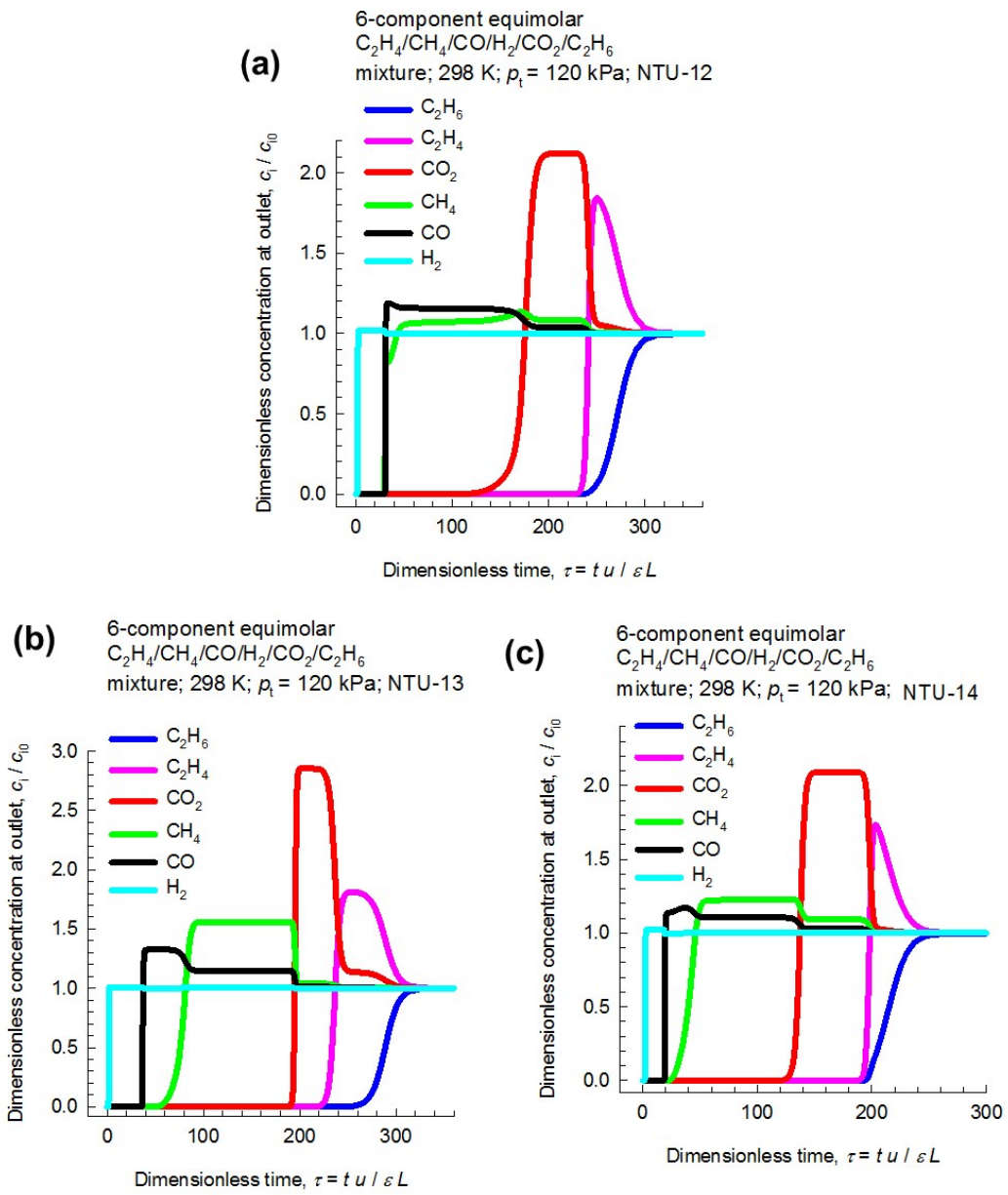

Fig. S53 Transient breakthrough simulations for separation of equimolar 6-component mixtures containing H_2, CH_4, CO, CO_2, C_2H_4, and C_2H_6 at 298 K using (a) **NTU-12**, (b) **NTU-13**, and (c) **NTU-14** at 298 K. The total inlet pressure is 120 kPa, with partial pressures of 20 kPa each.

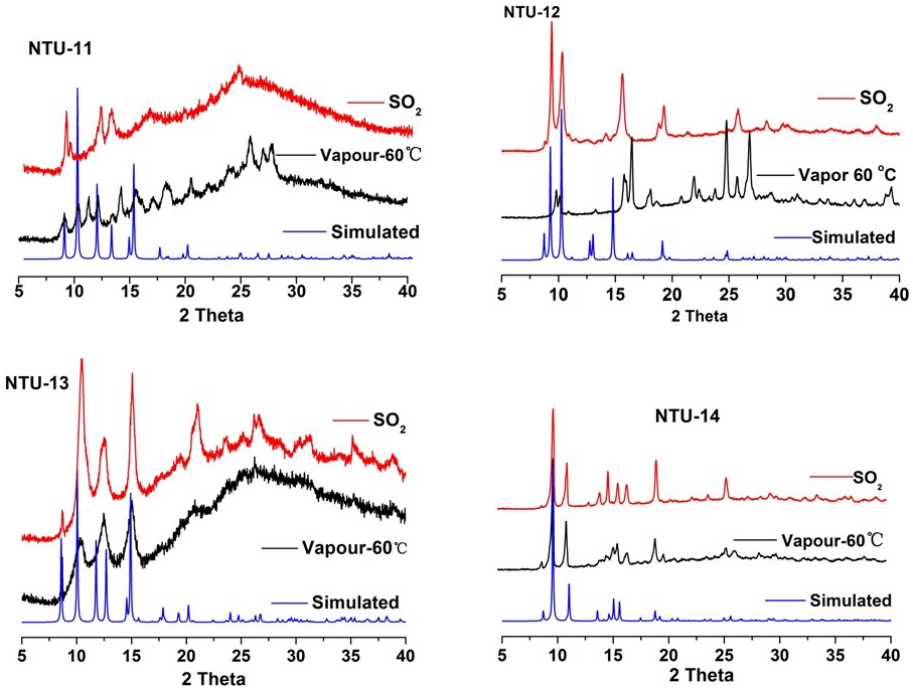

Fig. S54 PXRD of water vapor and SO_2 treated NTU-11 to -14. Fully activated PCPs were treated by water vapor (60℃) or SO_2 (25℃) for 24 h, respectively.

Membrane preparation

The **NTU-14** particles were dispersed in a solvent mixture of 70 wt % ethanol and 30 wt % water and then treated by ultrasonication and stirring for 1/2 h for three times each. The crystals were first ‘‘primed’’ by adding a certain amount of PEBA polymer and stirred for another 2 h at 80 ^{o}C (w PEBA: w EtOH/H_2O=1 : 100). Subsequently, the suspension containing primed particles was mixed with the remaining bulk polymer (w PEBA : w EtOH/H_2O = 4 : 100) and kept on stirring for another 2 h. After that, the solution kept at 60 ^{o}C overnight to eliminate trapped air bubbles. The hybrid composite membranes were cast on PVDF substrate using spin-coating method. Following removal of the solvent under room temperature for 24 h and then curing in the oven at 70 ^{o}C for 12 h, the **NTU-14** filled PEBA membrane was fabricated. Similarly using the PEBA solution (5 wt%) without mixed with NTU-14 particles, the unfilled PEBA membrane was prepared as described above. The loading in the membrane was calculated as following formula:

$$w_{PCP} = \frac{m_{PCP}}{m_{CS}} \times 100\% \quad (1)$$

where w_{MOF} is the particle loading, m_{MOF} and m_{PEBA} represent the weights of **NTU-14** and PEBA, respectively. The loading of these membranes in present study was 4 wt%.

Membrane Characterization

Gas transport performances were measured by gas permeation test using constant pressure/variable volume technique. For pure gas permeation tests of CO_2 and CH_4, the condition was set as 0.3 MPa at room temperature. After the system reached steady-state, all the gas permeation measurements were performed more than three times, and the gas permeance was calculated using the following equation:

$$P = \frac{Q}{\Delta P A}$$

where P is the gas permeance [1 GPU= 10^{-10} cm^3 (STP) /(cm^2 s cmHg)], Q is the volume permeate rate of gas (cm^3/s) at standard temperature and pressure (STP), ΔP is the transmembrane pressure (cmHg) and A is the effective membrane area (2.27 cm^2 in this work). The ideal selectivity of CO_2/CH_4 can be calculated by the ratio of the permeability of the individual gas which can be expressed as follows:

$$\alpha = \frac{P_A}{P_B}$$

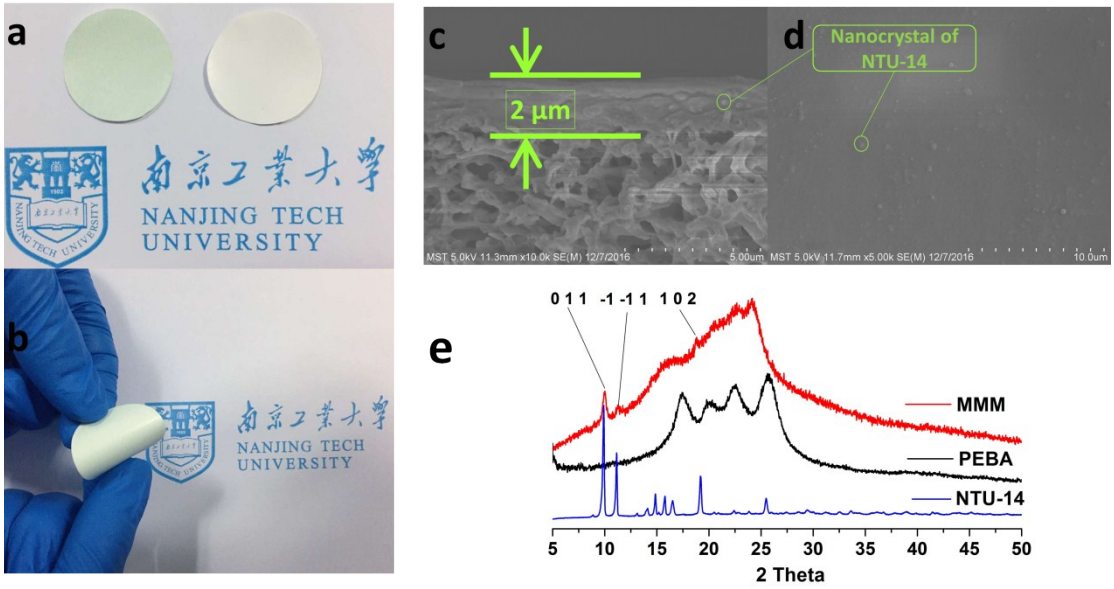

Fig. S55 Photo image of **NTU-14** MMM and pure PEBA membrane (a); flexibility of **NTU-14** MMM (b); SEM image of cross section of **NTU-14** MMM (c); SEM image of top view of **NTU-14** MMM (d); PXRD of **NTU-14** MMM (e).

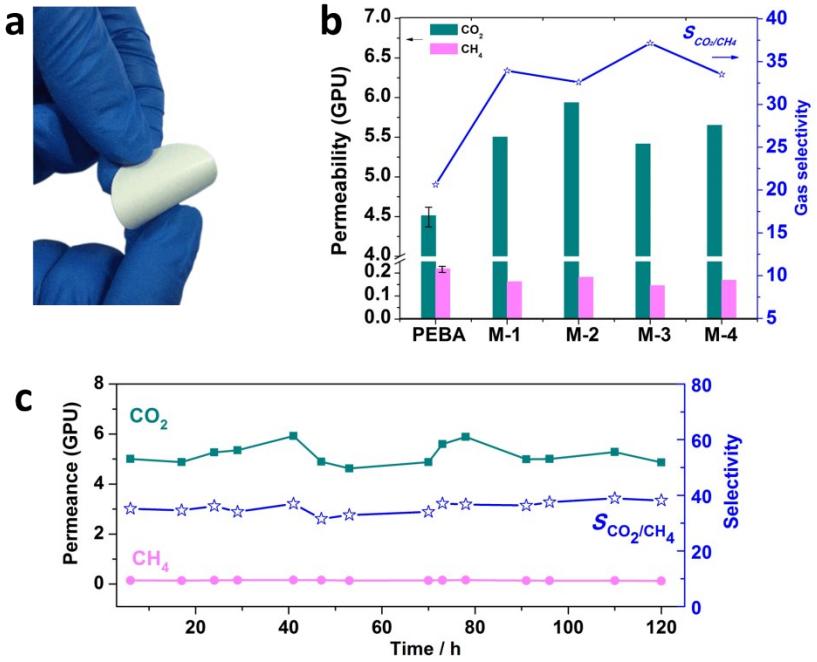

Fig. S56 View of flexible NTU-14/PEBA with light green colour (a), comparison of gas selectivity in PEBA and three MMMs (b), long term working of **NTU-14** MMM at room temperature (c).

Notation

b	Langmuir constant, Pa^{-1}
L	length of packed bed adsorber, m
p_i	partial pressure of species *i* in mixture, Pa
p_t	total system pressure, Pa
q_i	component molar loading of species *i*, mol kg^{-1}
q_t	total molar loading in mixture, mol kg^{-1}
q_{sat}	saturation loading, mol kg^{-1}
R	gas constant, 8.314 J mol^{-1} K^{-1}
t	time, s
T	absolute temperature, K
u	superficial gas velocity in packed bed, m s^{-1}
z	distance along the adsorber, and along membrane layer, m

Greek letters

□	voidage of packed bed, dimensionless
□	framework density, kg m^{-3}
□	time, dimensionless

Subscripts

i	referring to component *i*
t	referring to total mixture

Refs:

1 Sheldrick, G. M. A short history of SHELX. *Acta Crystallogr. Sec. A* **64**, 112-122, (2008).

2 Vandersluis, P. & Spek, A. L. Bypass - an Effective Method for the Refinement of Crystal-Structures Containing Disordered Solvent Regions. *Acta Crystallogr. Sec. A* **46**, 194-201, (1990).

3 Spek, A. L. Single-crystal structure validation with the program PLATON. *J. Appl. Crystallogr.* **36**, 7-13, (2003).

4 Krishna, R. The Maxwell-Stefan description of mixture diffusion in nanoporous crystalline materials. *Microporous Mesoporous Mater.* **185**, 30-50, (2014).

5 Krishna, R. Methodologies for evaluation of metal-organic frameworks in separation applications. *Rsc Adv* **5**, 52269-52295, (2015).

6 Krishna, R. Methodologies for Evaluation of Metal-Organic Frameworks in Separation Applications. *RSC Advances* **5**, 52269-52295, (2015).